



**HAL**  
open science

## Discrete anisotropic radiative transfer modelling of solar-induced chlorophyll fluorescence: Structural impacts in geometrically explicit vegetation canopies

Zbyněk Malenovský, Omar Regaieg, Tiangang Yin, Nicolas Lauret, Jordan Guilleux, Eric Chavanon, Nuria Duran, Růžena Janoutová, Antony Delavois, Jean Meynier, et al.

### ► To cite this version:

Zbyněk Malenovský, Omar Regaieg, Tiangang Yin, Nicolas Lauret, Jordan Guilleux, et al.. Discrete anisotropic radiative transfer modelling of solar-induced chlorophyll fluorescence: Structural impacts in geometrically explicit vegetation canopies. 2024. hal-04631496

**HAL Id: hal-04631496**

**<https://hal.science/hal-04631496v1>**

Preprint submitted on 2 Jul 2024

**HAL** is a multi-disciplinary open access archive for the deposit and dissemination of scientific research documents, whether they are published or not. The documents may come from teaching and research institutions in France or abroad, or from public or private research centers.

L'archive ouverte pluridisciplinaire **HAL**, est destinée au dépôt et à la diffusion de documents scientifiques de niveau recherche, publiés ou non, émanant des établissements d'enseignement et de recherche français ou étrangers, des laboratoires publics ou privés.



## Discrete anisotropic radiative transfer modelling of solar-induced chlorophyll fluorescence: Structural impacts in geometrically explicit vegetation canopies

Zbyněk Malenovský<sup>a,b,\*</sup>, Omar Regaieg<sup>c</sup>, Tiangang Yin<sup>b,d</sup>, Nicolas Sazret<sup>e</sup>, Jordan Guilleux<sup>c</sup>, Eric Chavanon<sup>c</sup>, Nuria Duran<sup>c</sup>, Růžena Janoutová<sup>c</sup>, Antony Delavoue<sup>c</sup>, Jean Meynier<sup>c</sup>, Ghania Medjdoub<sup>c</sup>, Peiqi Yang<sup>f</sup>, Christiaan van der Tol<sup>f</sup>, Douglas Morton<sup>g</sup>, Bruce Douglas Cook<sup>b</sup>, Jean-Philippe Gastellu-Etchegorry<sup>c</sup>

<sup>a</sup> School of Geography, Planning, and Spatial Sciences, College of Sciences Engineering and Technology, University of Tasmania, Private Bag 76, Hobart, TAS 7001, Australia

<sup>b</sup> NASA Goddard Space Flight Center, Biospheric Sciences Laboratory, 8800 Greenbelt Rd, Greenbelt, MD 20771, USA

<sup>c</sup> Centre d'Etudes Spatiales de la Biosphère - UTE, CNES, CNRS, IRD, Université de Toulouse, CNRS, Toulouse Cedex 9, France

<sup>d</sup> Earth System Science Interdisciplinary Center, University of Maryland, College Park, MD 20742, USA

<sup>e</sup> Global Change Research Institute of the Czech Academy of Sciences, Běldla 986/4a, 60300 Brno, Czech Republic

<sup>f</sup> Faculty of Geo-Information Science and Earth Observation (ITC), University of Twente, PO Box 217, Enschede 7500, the Netherlands

### ARTICLE INFO

Editor name: Jing M. Chen

#### Keywords

DART  
Fluspect  
SCOPE  
SIF  
Sun-/shade-adapted leaves  
LAI  
Clumping  
Wood

### ABSTRACT

Solar-induced fluorescence (SIF) is a subtle but informative optical signal of vegetation photosynthesis. Remotely sensed SIF integrates environmental, physiological and structural changes that alter photosynthesis at leaf, plant and canopy scales. Radiative transfer models are ideally suited to investigate the complex sources of variability in the SIF signal to enable the interpretation of SIF retrievals from airborne and space-borne platforms. Here, we coupled the FluSpec-Cx model of leaf optical properties and chlorophyll-a fluorescence with the Discrete Anisotropic Radiative Transfer (DART) model to upscale SIF from individual leaves to three-dimensional (3D) structurally explicit canopies. For two-dimensional homogeneous (turbid-like) canopies, DART-SIF was nearly identical to SIF simulated in two existing models, SCOPE and mSCOPE (RMSE <math>0.221 \text{ W}\cdot\text{m}^{-2}\cdot\mu\text{m}^{-1}\cdot\text{sr}^{-1}</math>). DART simulations in geometrically explicit 3D canopies offered four important insights regarding the influence of vegetation structure on the multi-angular top-of-canopy SIF signal. First, changes in the 3D canopy architecture of maize crops, represented by leaf density (leaf area index), and plant clumping (canopy closure) had a larger impact on SIF than the modelled photosynthetic efficiency distinction between sun-adapted and shade-adapted foliage. Second, clumping of leaves at the crop and stand levels was identified as one of the key driving factors of multi-angular anisotropy of red and far-red SIF (686 and 740 nm) for both maize and eucalyptus canopies. Third, non-photosynthetic woody material had a significant impact on top-of-canopy SIF in modelled 3D forest stands. Wood shadowing decreased the photosynthetically active radiation absorbed by green leaves, and consequently the SIF emissions, by 10% in sparse and 17% in dense eucalyptus stands. The wood obstruction (blocking) effect, quantified as a relative difference of SIF escape probabilities from canopies with and without wood in the nadir viewing direction, decreased far-red SIF by 4–6% but it had a smaller and sometimes positive influence (by less than 2%) on red SIF. Fourth, DART 3D radiative budget profiles revealed that the majority of the SIF signal from a dense eucalyptus stand originated from the top 25% of the simulated canopy. Interestingly, the introduction of bark-covered woody elements did not alter the simulated balance and omnidirectional escape factor of red SIF in this upper canopy part but did raise significantly both of them in case of far-red SIF. These results demonstrate the importance of 3D radiative transfer and radiative budget simulations for investigating SIF interactions in structurally complex plant canopies and for a better understanding of spatiotemporal and multi-angular remote sensing SIF observations.

\* Corresponding author at: School of Geography, Planning, and Spatial Sciences, College of Sciences Engineering and Technology, University of Tasmania, Private Bag 76, Hobart, TAS 7001, Australia.

E-mail address: [zbynek.malenovsky@gmail.com](mailto:zbynek.malenovsky@gmail.com) (Z. Malenovský).

<https://doi.org/10.1016/j.rse.2021.112564>

Received 18 September 2020; Received in revised form 10 May 2021; Accepted 14 June 2021

Available online 25 June 2021

0034-4257/© 2021 Elsevier Inc. All rights reserved.

### 1 **1. Introduction**

2 The potential for airborne and spaceborne monitoring of plant productivity has motivated  
3 optical remote sensing (RS) scientists since the launch of first Earth observing satellites (Ashley  
4 and Rea 1975; Blair and Baumgardner 1977). The faint signal of chlorophyll *a* fluorescence  
5 has been the target of vegetation RS for several decades (Rosema et al. 1991). Although recent  
6 technological advances in narrow-band imaging spectroscopy provide the first estimates of  
7 solar-induced chlorophyll fluorescence (SIF) from space (Frankenberg et al. 2011; Guanter et  
8 al. 2007; Joiner et al. 2011), the retrieval and use of the subtle SIF signal emitted in the red and  
9 near-infrared spectral regions to assess plant productivity is fraught with natural complexity of  
10 vegetated landscapes. Hence, RS applications of SIF, including physiological principles,  
11 instruments, measurement techniques and computer models (Mohammed et al. 2019), need a  
12 further development to improve our understanding and correct interpretation of the diurnal,  
13 seasonal, and interannual variabilities in the SIF signal observed with RS instruments at local,  
14 regional and global spatial scales. In particular, SIF variability originating from multiple  
15 scattering and reabsorption within structurally complex vegetation canopies is poorly  
16 understood, as are optical interactions in topographically rough and spatially heterogeneous  
17 natural and man-made landscapes (Zhang et al. 2020).

18 Radiative transfer modelling is a well-established and inseparable part of modern optical  
19 RS methods (Myneni and Ross 2012). Computer simulated radiative transfer in vegetation  
20 (Widlowski et al. 2015) has been used for local and global sensitivity analyses of various RS  
21 phenomena (e.g., Malenovský et al. 2008; Verrelst and Rivera 2017; Verrelst et al. 2010), and  
22 also for retrieval and interpretation of quantitative vegetation descriptors from remotely sensed  
23 spectral observations obtained through various inversion procedures (e.g., Croft et al. 2020;  
24 Malenovský et al. 2013; Verrelst et al. 2019). One of the most frequently used and well-  
25 established leaf-scale RTMs is PROSPECT (Féret et al. 2020; Féret et al. 2017; Jacquemoud  
26 and Baret 1990; Malenovský et al. 2006). Its first clone designed to simulate the chlorophyll-*a*  
27 fluorescence emission in plant leaves was FluorMODleaf (Pedrós et al. 2010), followed by  
28 computationally simpler Fluspect-B (Vilfan et al. 2016) and Fluspect-Cx (Vilfan et al. 2018).  
29 The Fluspect models reproduce leaf optical properties between 400 and 2500 nm together with  
30 3D matrices of forward- and backward-emitted SIF per wavelength of photosynthetically active  
31 radiation (PAR) incident on the adaxial side of a dark-adapted leaf. Besides these semi-  
32 empirical models, physical 3D leaf fluorescence RTMs have been developed, e.g., the Monte

33 Carlo (MC) Photon Transport (Sušila and Nauš 2007) or the Fluorescence Leaf Canopy Vector  
34 Radiative Transfer model (Kallel 2020). The MC models are, however, computationally  
35 demanding and, therefore, less suitable for an operational use in routine applications.

36 Models of SIF radiative transfer are developed hand-in-hand with the RS experimental  
37 work conducted at leaf as well as canopy scales (Aasen et al. 2019). Leaf RTMs are usually  
38 embedded in canopy-scale RTMs that can be classified according to the canopy representation  
39 as one-dimensional (1D) or three-dimensional (3D). Strengths and weaknesses of available  
40 canopy RTM types are reviewed in Malenovský et al. (2019). 1D models, such as SAIL  
41 (Verhoef 1984), were designed for a horizontally homogeneous canopy with structural, optical  
42 and biochemical variability only in the vertical dimension (e.g., mono-species crops). The most  
43 frequently used SIF model for 1D canopies is a SAIL's successor called SCOPE (van der Tol  
44 et al. 2009; van der Tol et al. 2019; Yang et al. 2020a), recently extended for multi-layered  
45 canopies as mSCOPE (Yang et al. 2017). Both SCOPE models are not modelling just radiance  
46 and SIF transfer but also soil-vegetation-atmosphere temperature and energy balances,  
47 including photosynthetic processes. SCOPE is frequently used for its simplicity and robustness,  
48 but its 1D architecture is unsuitable for complex multi-species ecosystems with structurally  
49 heterogeneous canopy layers and rough topography (e.g., boreal forests or savannas; Liu et al.  
50 2019a). Therefore, several 3D RTMs have been equipped with the ability to scale SIF from  
51 leaves to canopies to better capture the influence of structural heterogeneity of vegetation  
52 canopies. FluorWPS is a 3D MC ray-tracing SIF model (Zhao et al. 2016) that was developed  
53 and tested on 3D agricultural crops (Tong et al. 2021). Flux tracking of SIF simulated in the  
54 Discrete Anisotropic Radiative Transfer (DART) model (Gastellu-Etchegorry et al. 1996) was  
55 used to assess its multi-angular anisotropy in 3D maize canopies (Gastellu-Etchegorry et al.  
56 2017). The FluorFLIGHT 3D model, developed from FLIGHT (North 1996), supported  
57 assessment of Mediterranean oak forest water stress and *Phytophthora* infections from airborne  
58 SIF data (Hernández-Clemente et al. 2017). Finally, the FLiES MC model (Sakai et al. 2020)  
59 was used to interpret space-borne SIF of Amazonian forests (Köhler et al. 2018).

60 Despite the fact that all RTMs rely on simplifications and assumptions, they are powerful  
61 tools to investigate the optical interactions of SIF, which is needed for scaling and interpretation  
62 of the SIF signals acquired by proximal, airborne and spaceborne instruments (Bendig et al.  
63 2020; Gamon et al. 2019; Wyber et al. 2017). The main goal of this paper is to demonstrate the  
64 ability of the DART model coupled with Fluspect-Cx to assess the influence of canopy 3D

## 2.1 VEGETATION SIMULATED AS FACETS

65 architecture on the top-of-canopy SIF ( $SIF_{TOC}$ ) for cropland and forested environments that are  
66 difficult or even infeasible to investigate directly. DART simulations in this study address three  
67 primary research questions. First, in absence of a suitable 3D validation measurements and to  
68 verify their modelling consistency, do the DART, SCOPE and mSCOPE models provide  
69 comparable estimates of  $SIF_{TOC}$  for structurally homogenous vegetation in form of a turbid  
70 medium? Second, what is the  $SIF_{TOC}$  impact originating from biochemical leaf fluorescence  
71 efficiencies ( $f_{qe}$ ), varying for sun- and shade-adapted leaves, in comparison to increasing leaf  
72 density and clumping of maize (*Zea mays L.*) canopies? And third, what are the effects of woody  
73 trunks and branches on simulated  $SIF_{TOC}$ , SIF fluxes and escape factors from 3D forest  
74 abstractions of dense and sparse Australian white peppermint (*Eucalyptus pulchella*) stands?

## 75 2. Material and Methods

### 76 2.1 Implementation of leaf chlorophyll fluorescence in DART

77 We used the 3D DART model as the pilot RTM of this study. DART, being developed by  
78 researchers from the CESBIO Laboratory in Toulouse for more than 20 years (Gastellu-  
79 Etchegorry et al. 1996), was successfully cross compared with other state-of-the-art RTMs  
80 within the RAMI exercise (Widlowski et al. 2015). It produces at-sensor top-of-atmosphere  
81 (TOA) and bottom-of-atmosphere (BOA) multi-angular RS images by tracking optical and  
82 thermal photon fluxes through any type of 3D landscape with atmosphere (Gastellu-Etchegorry  
83 et al. 2015). Additionally, it calculates the quantitative 3D radiative budget, i.e., fluxes of  
84 intercepted, absorbed, reflected and emitted radiation, in the optical spectral domain (400-2500  
85 nm) (Gastellu-Etchegorry et al. 2004). The presence of woody material was implemented in  
86 DART in 2008 (Malenovský et al. 2008), and radiative transfer of Fluspect-Cx modelled SIF  
87 emissions in 2017 (Gastellu-Etchegorry et al. 2017). The Fluspect-Cx implementation followed  
88 the approach that was previously applied to couple DART with the PROSPECT-D model (Féret  
89 et al. 2017), taking advantage of both models' computational similarities and commonalities in  
90 input/output handling. The DART version 5.7.3, used in this work, simulates SIF radiative  
91 transfer and budget for 3D vegetation canopies constructed from geometrically explicit  
92 triangular objects (facets). Based on user-defined input parameters (i.e., leaf chlorophyll  $a+b$ ,  
93 total carotenoid and brown pigment contents, equivalent water thickness, dry leaf mass per area,  
94 leaf mesophyll structural parameter and specific fluorescence efficiencies), Fluspect generates  
95 four SIF matrices ( $M_{xyij}$ ), where  $x$  is the photosystem PSI or PSII,  $y$  is the backward or forward

96 direction relative to radiation incident direction,  $i$  is the 1 nm excitation band in the  
 97 photosynthetically active spectral region from 400 to 750 nm ( $i \in [1 \text{ I}]$ ), and  $j$  is the 1 nm emitted  
 98 SIF band ( $j \in [1 \text{ J}]$ ) in the spectral region from 640 to 850 nm. Consequently, the Fluspect SIF  
 99 leaf exitance ( $F_{xyj}$ ) at band  $j$  (1 nm bandwidth) due to irradiance ( $E_i$ ) in band  $i$  is:

$$100 \quad F_{xyj} = M_{xyij} \cdot E_i. \quad (1)$$

101 In contrast to Fluspect, DART works with any number of spectral bands that can have any  
 102 bandwidth, for example with U excitation bands  $\lambda_u$  and V fluorescence bands  $\lambda_v$ . Hence, in  
 103 DART, a leaf irradiance ( $E_u$ ) leads to the leaf exitance:

$$104 \quad F_{xyv} = M_{xyuv} \cdot E_u, \quad (2)$$

105 where  $M_{xyuv}$  is derived from the Fluspect matrices ( $M_{xyij}$ ) using an interpolation on spectral  
 106 bands ( $\Delta\lambda_u = \sum \alpha_{ui} \cdot \Delta\lambda_i$ ,  $\Delta\lambda_v = \sum \beta_{uj} \cdot \Delta\lambda_j$ ) and the two-step weighted arithmetic averaging:

$$107 \quad M_{xyuv} = \frac{\sum_j \beta_{uj} \cdot \Delta\lambda_j \cdot M_{xyuj}}{\sum_j \beta_{uj} \cdot \Delta\lambda_j}, \text{ where} \quad (3)$$

$$108 \quad M_{xyuj} = \frac{\sum_i \alpha_{ui} \cdot \Delta\lambda_i \cdot M_{xyij}}{\sum_i \alpha_{ui} \cdot \Delta\lambda_i}. \quad (4)$$

109 DART spectral leaf SIF exitance is accurate only if the  $u$  bands cover the entire SIF excitation  
 110 spectral interval and if they do not overlap. Similarly, it simulates the whole SIF domain only  
 111 if the  $v$  bands cover the whole SIF emission spectral interval.

112 The Fluspect calibration optical parameters (i.e., specific absorption coefficients, refractive  
 113 index of mesophyll cell walls and water, etc.) are stored in an external table called Optipar. We  
 114 used the Optipar table released in 2015. Additionally to the standard PROSPECT leaf  
 115 biochemical and structural inputs, Fluspect requires leaf fluorescence quantum efficiencies  
 116 ( $fqe$ ), in DART referred to as fluorescence yields, for PSI and PSII. The specification of  $fqe$   
 117 values in DART is flexible. They can be entered per individual foliage facet or specified as  
 118 general parameters that represent all leaves or a group of leaves in a given canopy. Biologically  
 119 meaningful foliage groups are, for instance, sunlit (i.e., leaves exposed to direct sun radiation)  
 120 and shaded leaves (i.e., leaves in the shadow of other phytoelements), or sun-adapted (i.e.,  
 121 leaves exposed most of the time to a direct sun radiation and subsequently adapting their  
 122 pigment pools for a high photoprotective capacity) and shade-adapted leaves (i.e., leaves  
 123 growing most of their lifespan under a low-intensity diffuse light and consequently having no  
 124 need for a high photoprotective capacity). It is important to keep in mind that a momentarily

## 2.1 VEGETATION SIMULATED AS FACETS

125 shaded leaf can actually be sun-adapted and vice versa, depending on its instantaneous and total  
126 diurnal illumination.

127 The implementation of DART chlorophyll fluorescence emission  $F_{xyv}$  (Eq. 2) does not  
128 account for the microclimatic conditions influencing the actual leaf photosynthetic activity.  
129 However,  $F_{xyv}$  can be in a vertical canopy profile additionally weighted by an *eta* parameter,  
130 which adjusts the leaf SIF exitance according to actual local temperature, humidity, wind  
131 aerodynamics and other microclimatic environmental conditions. Similar to *fqe*, the *eta* profile  
132 can be inserted either for a whole canopy, per a foliage group, or per pre-defined leaf groups.  
133 Since DART modelling does not contain soil-vegetation-atmosphere transfer (SVAT) of  
134 energy, the *eta* parameter must be precomputed out of DART with a SVAT model (e.g.,  
135 SCOPE; van der Tol et al. 2009) that considers dynamic meteorological factors as active parts  
136 in computation of the energy balance. DART simulates the total and the per-photosystem  
137  $SIF_{TOC}$  radiance and TOC reflectance using the N-flux tracking transfer. Technical details about  
138 the SIF flux tracking in DART are available in the DART User's Manual (Chapter III.2.2.d;  
139 DART 2020), while DART physical principles and mathematical descriptions are detailed in  
140 the DART Handbook (DART 2019).

### 141 **2.2 Comparison of DART and SCOPE/mSCOPE SIF radiative transfers**

142 In absence of a suitable empirical verification data, we compared the DART  $SIF_{TOC}$  signal  
143 with comparable outcomes produced by the SCOPE model and its multi-layer extension,  
144 mSCOPE (both in version 1.62). SCOPE is a broadly accepted model that has been previously  
145 confronted and validated with  $SIF_{TOC}$  measurements of agricultural crops (van der Tol et al.  
146 2016). It simulates vegetation canopy as a turbid medium of infinitely small leaves distributed  
147 in 60 horizontally homogeneous vertical layers (Yang et al. 2017), all of them with the same  
148 predefined leaf biochemical and canopy structural parameters. mSCOPE allows users to divide  
149 canopy into multiple horizontal layers and to assign to each one specific leaf optical properties  
150 and LAI. The methodology and graphical outputs of the DART and SCOPE/mSCOPE SIF  
151 radiative transfer comparison are, due to a large extent, provided in Appendix A.

### 152 **2.3 DART modelled influence of geometrically explicit plant canopy structures on SIF**

153 DART works with detailed and spatially explicit 3D representations of plant foliage and  
154 other canopy elements (e.g., trunks and branches), and can be, therefore, used to investigate  
155 how the structural components modulate the simulated  $SIF_{TOC}$  signal through optical photon

156 interactions as well as via foliage shading and physiological adaptations to prevailing  
 157 photosynthetic light intensity. For this purpose, we built two realistic but structurally different  
 158 mono-species canopies: i) an agricultural field of 1 m tall maize plants with eight leaves, created  
 159 with the open source graphical software Blender (Blender 2007) according to a template  
 160 produced by the plant architecture modelling L-system OpenAlea (Pradal et al. 2008), and ii) a  
 161 16 m tall forest stand of white peppermint trees, created from terrestrial laser scans of real trees  
 162 (Janoutová et al. 2019) growing in southern Tasmania (Australia). 3D landscapes were built as  
 163 juxtaposed scenes located at the same Latitude of 39.03°N and Longitude of 76.85°W  
 164 (Maryland, USA) as previous simulations, with the solar angles for 10<sup>th</sup> July 2014 for the test  
 165 of foliage sun and shade adaptation and for 26<sup>th</sup> August 2014 at 14.00 of local time (without the  
 166 daylight saving) for tests of maize canopy clumping and eucalypt wood influence. All canopies  
 167 were illuminated by the same DART-simulated BOA direct and diffuse solar irradiance, as  
 168 described in the previous section 2.2. Ground of the 3D scenes was optically defined as the  
 169 Lambertian loamy gravel brown dark soil with a linearly increasing reflectance ( $\rho \approx 6\%$  at 550  
 170 nm,  $\rho \approx 12\%$  at 686 nm and  $\rho \approx 15\%$  at 740 nm).

### 171 2.3.1 Distinction and influence of sun- and shade-adapted foliage in maize crops

172 As explained by Nobel (1976) or Givnish (1988), leaves growing in a shaded environment  
 173 are biochemically and anatomically different from those exposed for most of the day to direct  
 174 solar irradiation. DART users can consider these differences and their influence on SIF<sub>TOC</sub> by  
 175 classifying the facets of 3D vegetation leaves in several classes, for which leaf optical or  
 176 biochemical properties (including *fqe* and *eta* parameters) can be defined separately. The final  
 177 number of classes depends on the structural complexity of canopies and the availability of  
 178 measurements to support the detailed foliar parameterization. A simple two-class classification  
 179 would split leaf facets into just sun- and shade-adapted cohorts (DART 2020), considering a  
 180 long-term cumulative leave irradiance as the main driving force.

181 DART calculates intercepted, absorbed, reflected and emitted radiation, i.e. radiative  
 182 budget, per 3D cell of the simulated scene and also for each surface facet in the scene (Gastellu-  
 183 Etchegorry 2008), which can be used to distinguish between the sun- and shade-adapted leaf  
 184 cohorts. The intercepted radiation flux  $E(\lambda)$  [ $\text{W}\cdot\text{m}^{-2}$ ] can be converted into photosynthetic  
 185 photon flux density Q (PPFD) [ $\mu\text{mol}\cdot\text{photons}\cdot\text{m}^{-2}\cdot\text{s}^{-1}$ ] by integrating the intercepted PAR  
 186 (iPAR) per leaf facet as follows:

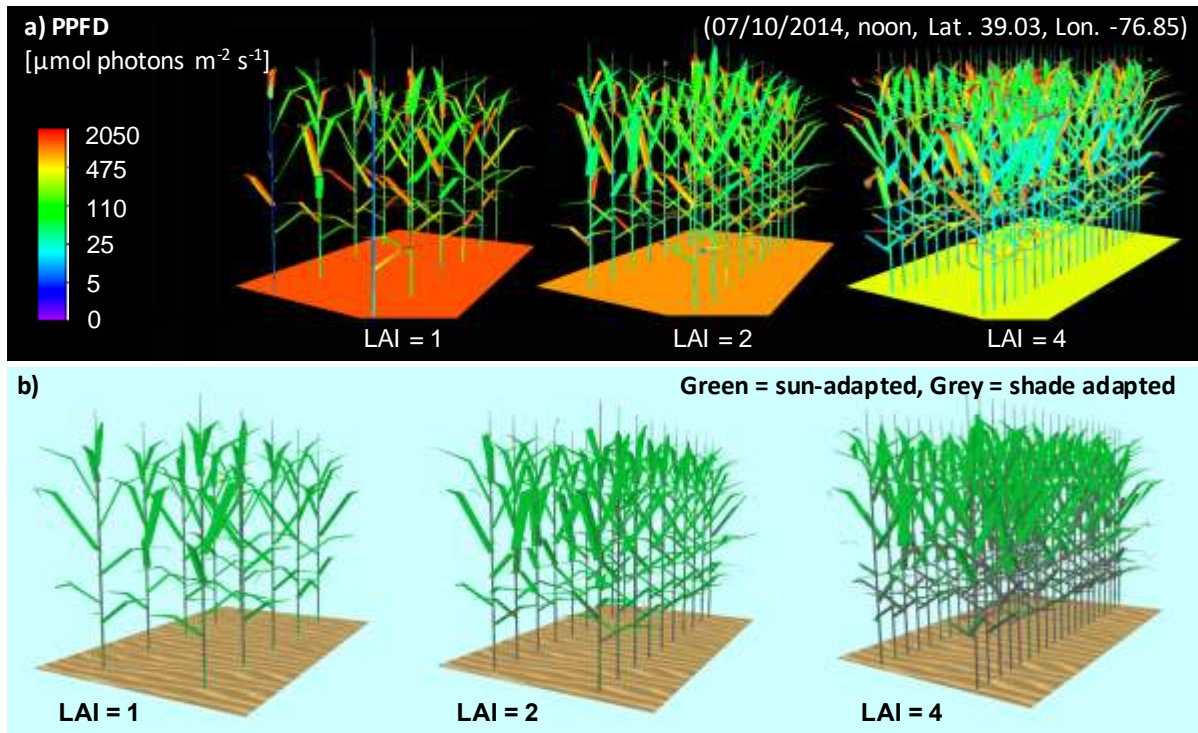


## 2.1 VEGETATION SIMULATED AS FACETS

$$187 \quad Q = \int_{\Delta\lambda_i} E(\lambda) \cdot d\lambda \cdot \frac{\int_{0.4\mu m}^{0.75\mu m} L_B(T, \lambda) \cdot \frac{\lambda \cdot 10^6}{h \cdot c \cdot N_a} \cdot d\lambda}{\int_{0.4\mu m}^{0.75\mu m} L_B(T, \lambda) \cdot d\lambda}, \quad (5)$$

188 where  $L_B(T, \lambda)$  is Planck's law at temperature  $T$  ( $T = 5800$  K) and wavelength  $\lambda$  [ $\mu\text{m}$ ],  $h$  is  
 189 Planck's constant [J.s],  $c$  is speed of light [ $\text{m}\cdot\text{s}^{-1}$ ],  $N_a$  is Avogadro's constant [ $\text{mole}^{-1}$ ], and  $\int_{\Delta\lambda_i}$   
 190 is the PAR spectral range from 400 to 750 nm. The  $Q$  value depends on the ratio of direct and  
 191 diffuse irradiance spectrum, leaf optical properties and PAR multiple scattering. Influenced by  
 192 literature findings about the potential of  $Q$  for differentiating sun- and shade-adapted leaves  
 193 (Leuning et al. 1995; Niinemets et al. 2015), the following two classification algorithms were  
 194 designed: i) a frequency double-threshold and ii) a probability distribution approach. Both  
 195 methods are based on simulated leaf PAR irradiance values for  $T$  time steps during  $i$  days, with  
 196  $T$  being small enough to ensure an adequate angular sampling of leaf irradiance variation during  
 197 the simulated days.

198 The first double-threshold approach asks user to specify high  $Q_H$  and low  $Q_L$  classification  
 199 thresholds. The facets are then categorized at each time step  $T$  into the three groups: i)  $H$  for  
 200  $Q > Q_H$ , ii)  $L$  for  $Q < Q_L$ , and iii)  $M$  for  $Q_H > Q > Q_L$ . The number of occasions when a leaf  
 201 facet appeared in each of these groups during the simulated day  $i$  is counted, resulting in [ $N_{H,i}$ ,  
 202  $N_{M,i}$ ,  $N_{L,i}$ ] with  $N_{H,i} + N_{M,i} + N_{L,i} = T$ . Subsequently, a leaf facet is labelled as sun-adapted  
 203 (i.e.,  $C_{f,i} = 1$ , with  $f \in [1, F]$  where  $F$  is the total number of leaf facets) if: i)  $N_{H,i} > \frac{T}{2}$  (i.e., leaf  
 204 facet is categorized as sunlit for the majority of the  $T$  time steps), or ii)  $N_{M,i} > \frac{T}{2}$  and  $N_{H,i} >$   
 205  $N_{L,i}$  (i.e., leaf irradiance is, for the majority of  $T$  time steps, between the two thresholds and a  
 206 leaf facet is categorized as sunlit more frequently than shaded). Finally, a leaf facet is labelled  
 207 as shade-adapted (i.e.,  $C_{f,i} = 0$ ) in all other cases, which cover the following three conditions:  
 208 i)  $N_{L,i} > \frac{T}{2}$ , ii)  $N_{M,i} > \frac{T}{2}$  and  $N_{H,i} < N_{L,i}$ , and iii) none of the [ $N_{H,i}$ ,  $N_{M,i}$ ,  $N_{L,i}$ ] values dominates  
 209 during the simulated times. This way, a day series (an array of  $i$  values) of sun-adapted ( $C_{f,i} =$   
 210 1) and shade-adapted ( $C_{f,i} = 0$ ) states is generated per leaf facet  $f$ . The final class assignment  
 211 is decided based on the median value of  $C_f$  across the entire examined time period.



212

213 Figure 1. Incident photosynthetically active radiation expressed in photosynthetic photon flux density  
 214 (PPFD) for three realistic 3D maize (*Zea mays L.*) canopies with LAI equal to 1, 2 and 4 (a). Distinction  
 215 of sun- (green) and shade- (grey) adapted foliage based on double PPFD thresholds of 50 and 100  
 216  $\mu\text{mol.photons.m}^{-2}.\text{s}^{-1}$  (b). To mimic realistic maize canopies, all three maize fields (1x1.5 m in size)  
 217 were created with 1 m tall semi-randomly oriented plants, having eight fully developed bifacial leaves.  
 218

218

219 The second method uses the probability distribution of the simulated diurnal Q time series.  
 220 The range of Q values is divided into equally or unequally distributed  $X$  intervals, and the Q  
 221 values of leaf facets simulated at each time step  $T$  are categorized in a group  $x$  ( $x \in [1, X]$ ). The  
 222 probability distribution functions of  $i \cdot T$  sampling points are then computed over  $x$  groups,  
 223 resulting in the maximum occurrence (i.e., the highest probability density) in group  $x_{\text{max}}$  and  
 224 the median occurrence in group  $x_{\text{median}}$ . A leaf facet is assigned as sun-adapted if  $x_{\text{max}} > \frac{x}{3}$   
 225 and  $x_{\text{max}} \leq x_{\text{median}}$ , and shade-adapted in all other cases. Both methods are available in the  
 226 DART toolbox directory as Python scripts, the decision which to use is solely of user discretion.  
 227

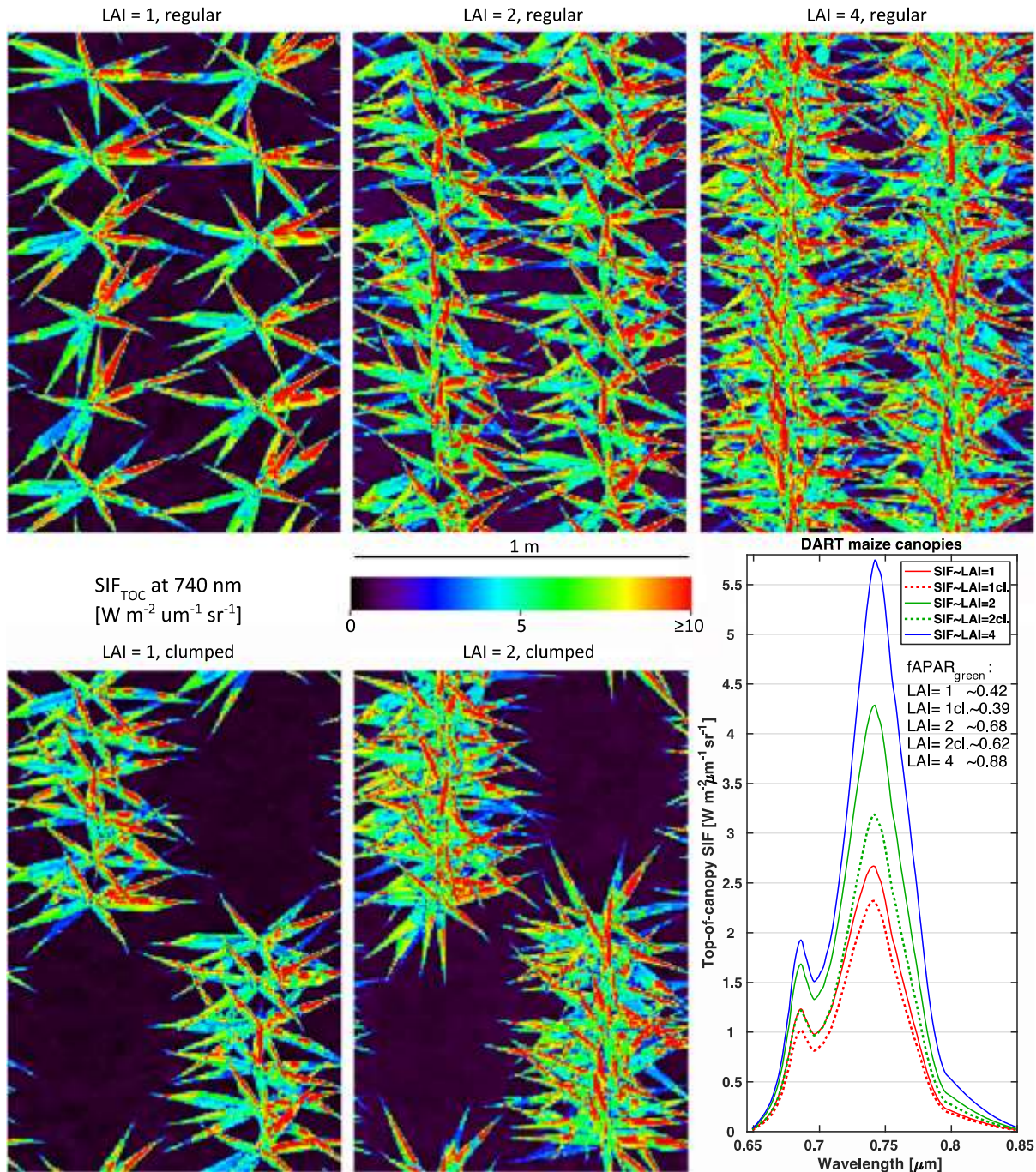
228 To demonstrate changes in  $\text{SIF}_{\text{TOC}}$  due to the distinction of sun- and shade-adapted leaves,  
 229 we applied two double-threshold classifications on three maize fields (Figure 1). The first  
 230 ‘relaxed’ classification used relatively high and far-apart thresholds of 50 and 100  
 231  $\mu\text{mol.photons.m}^{-2}.\text{s}^{-1}$ , allowing for a larger portion of shade-adapted parts, whereas the second  
 232 ‘strict’ classification used low and close thresholds of 15 and 25  $\mu\text{mol.photons.m}^{-2}.\text{s}^{-1}$ , resulting  
 in a smaller amount of strictly shade-adapted leaves and stems. The regularly spaced 1 m tall

## 2.1 VEGETATION SIMULATED AS FACETS

233 plants with fully developed bifacial leaves were placed in fields (1x1.5 m in size) with a random  
 234 geographical orientation and distances resulting in LAI = 1, 2 and 4. Specific leaf biochemical,  
 235 structural and fluorescence properties were assigned to each leaf adaptation class as listed in  
 236 Table 1 (note that foliage of scenarios without distinct light adaptations was assumed to have  
 237 the properties of sun-adapted leaves and stems). Contrary to previous SIF simulations, PSII *fqe*  
 238 values of medium magnitude were assigned to each leaf class, while PSI *fqe* values were kept  
 239 constant under the assumption that PSI contributes to SIF signal of both leaf types equally (Liu  
 240 et al. 2019a). In order to prevent its confounding effect, the energy balance (leaf photosynthesis)  
 241 modelling was disregarded, i.e., the fluorescence efficiency weight *eta* was forced to one. The  
 242 remaining inputs were arbitrarily defined within plausible dynamic ranges of published  
 243 laboratory measurements (Hosgood et al. 1994; Jacquemoud and Baret 1990).

244 Table 1. Input parameters of the Fluspect-Cx model to simulate optical properties of sun- and shade-  
 245 adapted leaves, as well as foliage without light adaptations and stems: content of chlorophyll *a+b* (Cab),  
 246 total content of carotenoids (Car), equivalent water thickness (EWT), leaf mass per area (LMA),  
 247 mesophyll optical thickness number (N) and fluorescence quantum efficiencies (*fqe*) for PSI and PSII.

Fluspect inputs	Cab [ $\mu\text{g}\cdot\text{cm}^{-2}$ ]	Car [ $\mu\text{g}\cdot\text{cm}^{-2}$ ]	EWT [cm]	LMA [ $\text{g}\cdot\text{cm}^{-2}$ ]	N	PSI <i>fqe</i>	PSII <i>fqe</i>
Sun-adapted and without adaptation leaves and stems	50	15	0.009	0.0021	1.5	0.002	0.016
Shade-adapted leaves and stems	75	20	0.012	0.0028	2.0	0.002	0.022



248

249 Figure 2. DART simulated images of top-of-canopy SIF at 740 nm for maize fields of three leaf area  
 250 indices (LAI) and two canopy closures, 100% regular (top) and 50% clumped (bottom), given by the  
 251 number of plants (LAI = 1 ~ 12 plants, LAI = 1 ~ 24 plants and LAI = 4 ~ 50 plants) associated with  
 252 different plant distances. The graph (bottom-right) displays the corresponding modelled canopy SIF  
 253 spectra between 650 and 850 nm and provides the fAPAR<sub>green</sub> values per scenario.

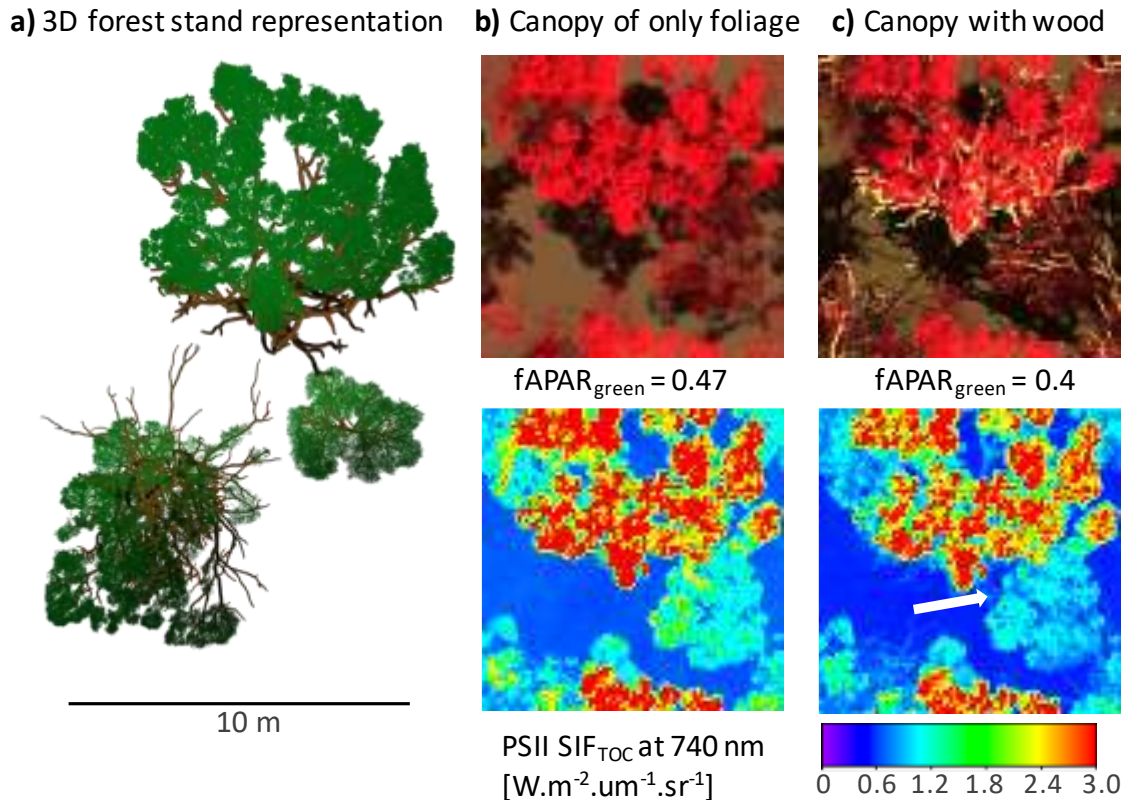
254 *2.3.2 Canopy SIF changes due to leaf density and clumping of maize plants*

255 Potential variability in SIF<sub>TOC</sub> due to leaf density and plant clumping (i.e., canopy closure  
 256 – CC) changes were simulated for virtual maize canopies of three plant densities (LAI = 1, 2



## 2.1 VEGETATION SIMULATED AS FACETS

257 and 4) in a regular spatial distribution ( $CC \approx 100\%$ ) and in two clumped formations (LAI = 1  
258 and 2,  $CC \approx 50\%$ ) (Figure 2). Compared to the previous exercise (Figure 1), distances between  
259 6 (LAI = 1) or 12 (LAI = 2) of neighbouring regularly spaced plants in a row were shortened  
260 by half to create regular foliage clumps and canopy gaps of the same size. To keep consistency,  
261 the leaf and stem optical properties were those used for the turbid-like canopies (Table A1) and  
262 the sun- and shade-adaptations were not distinguished, i.e., all leaves were considered as equal.



263

264 Figure 3. Nadir view of 3D representation of the dense white peppermint (*Eucalyptus pulchella*) test  
265 canopy derived from terrestrial laser scans of trees growing east of Hobart (Tasmania, Australia) (a).  
266 The virtual scene (LAI = 2) was used to simulate a near-infrared, red and green RGB false colour  
267 composite images in DART of top-of-canopy reflectance (top) as well as PSII SIF at 740 nm (bottom)  
268 of the canopy formed by: b) only foliage and c) foliage and woody material covered with bark. The  
269 white arrow points at the example of SIF reflection from an exposed tree branch surface.

### 270 2.3.3 Influence of leaf clumping, trunks and branches on SIF of white peppermint canopies

271 DART simulations of eucalyptus forest canopies were used to investigate potential impacts  
272 of leaf clumping and woody material, i.e., trunks and branches covered by bark, on SIF<sub>TOC</sub>  
273 modelled at 686 and 740 nm. 3D representations of the eucalyptus trees were constructed based  
274 on 3D point clouds acquired with the terrestrial laser scanner (TLS) Trimble TX8 (Trimble Inc.,  
275 USA). Three native white peppermint eucalypts of different age, height and general habitus

276 were scanned from several geolocations in dry sclerophyll forest located southeast of Hobart  
 277 (Tasmania, Australia) to acquire their TLS point clouds with a point spacing of 11.3 mm at  
 278 distance of 30 m. The TLS points of each tree were, after a mandatory pre-processing, semi-  
 279 automatically separated in two groups: i) points of trunks and branches and ii) points  
 280 representing foliage. Points classified as wood were used as attractors in an automatic procedure  
 281 (Sloup 2013) to extract the external surfaces of trunks and main branches, as described in  
 282 Verroust and Lazarus (1999). The foliage points were subsequently spatially collocated with  
 283 the reconstructed wooden skeleton. 3D representation of leaves was created in Blender (Blender  
 284 2007) based on an average shape and size of actual leaves and then distributed automatically at  
 285 the locations of foliage points according to the Erectophile LAD (Danson 1998), targeting two  
 286 crown LAI values of 2 and 5. A complete description of this TLS-based 3D construction of  
 287 trees, developed specifically for RTM purposes, is available in Janoutová et al. (2019). Two  
 288 DART canopies (scenes), were constructed with the 3D tree representations: i) a dense canopy  
 289 was created by placing three trees with the individual crown LAI = 2 within a scene of 81 m<sup>2</sup>,  
 290 while keeping CC ≈ 80% (Figure 3a), and ii) a sparse canopy was built by redistributing the  
 291 same trees but with the crown LAI = 5 within a scene of 196 m<sup>2</sup> to achieve CC ≈ 40%.  
 292 Combinations of the tree crown LAI and scene sizes ensured that both scenes had, for the  
 293 purpose of comparability, the same canopy LAI = 2.5. Additionally, an identical bark  
 294 directional-hemispherical reflectance ( $\rho \approx 20\%$  at 550 nm,  $\rho \approx 40\%$  at 686 nm and  $\rho \approx 50\%$  at  
 295 740 nm), measured on actual bark samples collected in field, was applied in both canopies.

296 Besides standard forest canopies (e.g., Figure 3c), the virtual environment of the DART  
 297 model also allows for simulating canopies composed of only foliage without woody  
 298 components (Figure 3b). By comparing results from simulations with and without woody  
 299 material, we quantified the magnitudes of shading and direct obstructing effects of woody  
 300 material. Removing woody components increases the within-canopy iPAR (Q) due to the  
 301 reduction in wood shadowing, which in turn increases SIF emitted by all previously shaded  
 302 leaves. The obstruction impact of woody material is caused by its optical interactions with SIF  
 303 photons. First, it diminishes (blocks) the within-canopy SIF at both 686 and 740 nm via bark  
 304 scattering and absorption. Second, it affects, to some extent, SIF emission through reflection of  
 305 SIF at 686 nm that can be reabsorbed and later reemitted by chlorophyll pigments.

#### 306 **2.4 Computation of canopy $fAPAR_{green}$ , SIF balance, escape factors and differences**

## 2.1 VEGETATION SIMULATED AS FACETS

307 The main driver of green foliage SIF emissions (including stems of the maize plants) in  
 308 DART simulations that do not contain a modulation of PSI and PSII *fqe* values by *eta*  
 309 coefficients is the fraction of absorbed photosynthetically active radiation (fAPAR<sub>green</sub>).  
 310 Therefore, a change of fAPAR<sub>green</sub> in these simulations indicates a change in the ratio of sunlit  
 311 and shaded photosynthetically active plant parts, which results in an equal relative change in  
 312 SIF leaf emission of both photosystems. To be able to investigate the impact of different 3D  
 313 canopy architectures on their fAPAR<sub>green</sub>, we calculated fAPAR<sub>green</sub> for all SIF<sub>TOC</sub> simulating  
 314 scenarios from the DART radiative budget of a single broad PAR band ( $\lambda = [400\ 750]$  nm) as:

$$315 \quad \text{fAPAR}(\lambda)_{\text{green}} = \frac{\text{APAR}(\lambda)_{\text{green}}}{\text{PAR}(\lambda)_{\text{TOC}}}, \quad (6)$$

316 where APAR( $\lambda$ )<sub>green</sub> is PAR absorbed by all green plant constituents of a given DART scene  
 317 and PAR( $\lambda$ )<sub>TOC</sub> is the solar incoming PAR simulated at the top of canopy. The relative  
 318 difference [%] in fAPAR<sub>green</sub> of clumped (C) compared to regularly spaced (R) maize canopies  
 319 was calculated as:

$$320 \quad \varepsilon_{\text{fAPAR}(\lambda)} = 100 \cdot \frac{\text{fAPAR}(\lambda)_{\text{green}_C} - \text{fAPAR}(\lambda)_{\text{green}_R}}{\text{fAPAR}(\lambda)_{\text{green}_R}}. \quad (7)$$

321 Similarly, the shading effect of woody components on eucalyptus SIF emissions was assessed  
 322 through the relative difference [%] of canopy fAPAR<sub>green</sub> obtained for simulations containing  
 323 just foliage (F) and foliage with wood (FW) as follows:

$$324 \quad \varepsilon_{\text{fAPAR}(\lambda)} = 100 \cdot \frac{\text{fAPAR}(\lambda)_{\text{green}_F} - \text{fAPAR}(\lambda)_{\text{green}_{FW}}}{\text{fAPAR}(\lambda)_{\text{green}_{FW}}}. \quad (8)$$

325 DART-simulated 3D radiative budget of SIF allows for locating origins of remotely sensed  
 326 SIF using the SIF balance (SIF( $\lambda$ )<sub>bal</sub>) [ $\text{W} \cdot \text{m}^{-2} \cdot \mu\text{m}^{-1}$ ], computed by subtracting the absorbed SIF  
 327 flux from the total emitted SIF flux (i.e., SIF( $\lambda$ )<sub>PSI</sub> plus SIF( $\lambda$ )<sub>PSII</sub>) of a given wavelength ( $\lambda$ )  
 328 per a vertical canopy layer. A positive SIF( $\lambda$ )<sub>bal</sub> means that the canopy layer acts as a SIF source,  
 329 while a negative SIF( $\lambda$ )<sub>bal</sub> indicates canopy parts acting as SIF sinks. Subsequently, relative  
 330 difference [%] of SIF( $\lambda$ )<sub>bal</sub> between clumped (C) and regularly spaced (R) maize canopies,  
 331 computed as:

$$332 \quad \varepsilon_{\text{SIF}(\lambda)_{\text{bal}}} = 100 \cdot \frac{\text{SIF}(\lambda)_{\text{bal}_C} - \text{SIF}(\lambda)_{\text{bal}_R}}{\text{SIF}(\lambda)_{\text{bal}_R}}, \quad (9)$$

333 reveals if the maize foliage clumping causes a further reduction ( $\varepsilon_{\text{SIF}(\lambda)_{\text{bal}}} < 0$ ) or an  
 334 enhancement ( $\varepsilon_{\text{SIF}(\lambda)_{\text{bal}}} > 0$ ) or no change ( $\varepsilon_{\text{SIF}(\lambda)_{\text{bal}}} = 0$ ) of SIF balance per a canopy layer.

335 The proportion of SIF photons that exit the top of canopy is described by the SIF<sub>TOC</sub> escape  
 336 probability factor (SIF<sub>esc</sub>). In practice, this is the ratio of SIF photons escaping from the top of  
 337 canopy in any direction to all SIF photons emitted from all canopy leaves in forward or  
 338 backward directions (Guanter et al. 2014). SIF<sub>esc</sub> is required for scaling of SIF<sub>TOC</sub> measurements  
 339 down at the spatial level of individual leaves (van der Tol et al. 2019), and subsequently  
 340 essential for correct estimation of vegetation gross primary production (GPP) from airborne and  
 341 spaceborne SIF observations (e.g., He et al. 2017; Zhang et al. 2020). Since most of RS  
 342 observations capture SIF<sub>TOC</sub> from nadir, we computed the relative canopy SIF escape  
 343 probability factor of a given wavelength ( $\lambda$ ) in the nadir direction (SIF<sub>nadir</sub>( $\lambda$ )<sub>esc</sub>) from SIF  
 344 radiative budgets of the eucalyptus scenarios. First, we converted SIF emissions of PSI and PSII  
 345 per m<sup>2</sup> of abaxial and adaxial leaf facets into SIF emissions per m<sup>2</sup> of the scene ( $F(\lambda)_{\text{PSI}}$  and  
 346  $F(\lambda)_{\text{PSII}}$ ) [W.m<sup>-2</sup>. $\mu\text{m}^{-1}$ ] and then calculated SIF<sub>nadir</sub>( $\lambda$ )<sub>esc</sub> as:

$$347 \quad \text{SIF}_{\text{nadir}}(\lambda)_{\text{esc}} = \frac{\pi \cdot (L_{\text{nadir}}(\lambda)_{\text{PSI}} + L_{\text{nadir}}(\lambda)_{\text{PSII}})}{F(\lambda)_{\text{PSI}} + F(\lambda)_{\text{PSII}}}, \quad (10)$$

348 where  $L_{\text{nadir}}(\lambda)_{\text{PSI}}$  and  $L_{\text{nadir}}(\lambda)_{\text{PSII}}$  [W.m<sup>-2</sup>. $\mu\text{m}^{-1}$ .sr<sup>-1</sup>] are DART modelled PSI and PSII SIF  
 349 radiances at the wavelength ( $\lambda$ ), respectively, escaping from the simulated scene in the nadir  
 350 viewing direction. The  $\pi$  multiplication in Eq. 10 is removing the angular dependency [sr<sup>-1</sup>],  
 351 resulting in relative values of SIF<sub>nadir</sub>( $\lambda$ )<sub>esc</sub> between 0 and 1. Since the escape probability factor  
 352 is predominantly dependent on direct optical interactions with canopy elements that attenuate  
 353 an emitted SIF signal, we quantified the obstruction (blocking) effect of eucalyptus woody  
 354 components on canopy SIF in the nadir viewing direction through the relative difference [%]  
 355 of SIF<sub>nadir</sub>( $\lambda$ )<sub>esc</sub>, computed from the foliage only (F) and the foliage with wood (FW)  
 356 simulations as follows:

$$357 \quad \varepsilon_{\text{SIF}(\lambda)_{\text{esc}}} = 100 \cdot \frac{\text{SIF}_{\text{nadir}}(\lambda)_{\text{esc}_F} - \text{SIF}_{\text{nadir}}(\lambda)_{\text{esc}_{FW}}}{\text{SIF}_{\text{nadir}}(\lambda)_{\text{esc}_{FW}}}. \quad (11)$$

358 Finally, to analyse differences in SIF fluxes escaping from individual simulated canopy layers  
 359 in all directions (i.e., towards layers of the upper and lower hemispheres), we computed from  
 360 DART 3D radiative budget their relative omnidirectional escape factor (SIF<sub>omni</sub>( $\lambda$ )<sub>esc</sub>) as:

$$361 \quad \text{SIF}_{\text{omni}}(\lambda)_{\text{esc}} = \frac{(F(\lambda)_{\text{PSI}} + F(\lambda)_{\text{PSII}}) - (A(\lambda)_{\text{PSI}} + A(\lambda)_{\text{PSII}})}{F(\lambda)_{\text{PSI}} + F(\lambda)_{\text{PSII}}}, \quad (12)$$

362 where  $A(\lambda)_{\text{PSI}}$  and  $A(\lambda)_{\text{PSII}}$  [W.m<sup>-2</sup>. $\mu\text{m}^{-1}$ ] are DART modelled absorptances of PSI and PSII SIF,  
 363 respectively, expressed for the wavelength ( $\lambda$ ) per m<sup>2</sup> of the scene. If SIF<sub>omni</sub>( $\lambda$ )<sub>esc</sub>  $\leq$  0, then



## 2.1 VEGETATION SIMULATED AS FACETS

364 the canopy layer does not contribute to the  $SIF_{TOC}$  signal, i.e., its  $SIF(\lambda)_{bal}$  is either neutral or  
365 negative.

### 366 *2.5 DART settings common to all SIF canopy simulations*

367 DART simulations were carried out with the flux-tracking algorithm using the following  
368 settings: no elimination of low energy rays, relative accuracy on scene albedo equal to  $10^{-6}$ , 25  
369 duplications of the initially simulated scene, the scene illumination mesh size equal to  $5 \cdot 10^{-4}$  m  
370 (with a semi-random spatial distribution of illumination rays), and cell sub-sampling with  $8^3$   
371 sub-cells per cell and 1 sub face per cell face. An optimal number of 20 flux-tracking iterations,  
372 which were required to obtain a  $10^{-2}$  relative accuracy of the scene reflectance, was determined  
373 through a simplified accuracy sensitivity study. Intermediate results of the last few iterations  
374 were used to extrapolate the final values of simulated radiative budget, bidirectional reflectance  
375 function and SIF products. TOC reflectance and SIF were simulated in 212 viewing directions  
376 (Yin et al. 2013), distributed systematically throughout the upward hemisphere, with an  
377 oversampling of the upward hot-spot region (25 directions in a solid angle of 0.01 sr around the  
378 hotspot direction) and 34 virtual viewing directions in the solar principle plane. Leaf facets  
379 were simulated as double-faces without the solar penumbra effect, all optical properties were  
380 assumed to be Lambertian, and the scene ground surface was horizontal.

### 381 *2.6 Comparative statistical indicators*

382 Comparative statistical indicators, specifically a root mean square error (RMSE) and an  
383 index of agreement (d), were computed to assess these similarities as well as anticipated  
384 statistical dissimilarities between different DART scenarios (i.e., turbid-like vs. maize and  
385 eucalypt canopies). As explained in Willmott (1981), the dimensionless index of agreement  
386 complements the RMSE by indicating the degree of correspondence between two tested  
387 datasets in magnitude and direction, where  $d = 1$  means full agreement and  $d = 0$  means total  
388 disagreement. Also, the similarity of DART and SCOPE multi-angular  $SIF_{TOC}$  was assessed  
389 through fitting a linear regression model, where the regression coefficient of determination ( $R^2$ )  
390 indicated how much of the variability in a reference RT model (i.e., SCOPE) results can be  
391 explained by corresponding regressed values simulated in DART.

## 392 **3. Results**

### 393 **3.1 Comparison of nadir DART and SCOPE/mSCOPE canopy SIF simulations**

394 The SCOPE and DART nadir SIF<sub>TOC</sub> signatures of turbid medium vegetation canopies  
 395 were nearly identical (Figure A2). Results between 641 and 850 nm were comparable for all  
 396 simulated input combinations (i.e., three LAI, three LAD and three soil types). High SIF<sub>TOC</sub>,  
 397 observed for canopies of Planophile LAD, is caused by their high PAR interception efficiency.  
 398 The highest RMSE = 0.162 W.m<sup>-2</sup>.μm<sup>-1</sup>.sr<sup>-1</sup> and the lowest d = 0.9965 were found for the  
 399 Erectophile canopy of LAI = 1, covering soil with ρ = 50%. Despite being the worst case, the  
 400 values indicate only minor differences between DART and SCOPE results. Statistical analyses  
 401 revealed that the total SIF<sub>TOC</sub> RMSE originates mainly from RMSE for PSII, which was twice  
 402 the RMSE for PSI simulations for all three LADs (results not shown). Despite a significantly  
 403 higher variability in RMSE than other two LADs, the Planophile LAD showed the highest index  
 404 of agreement and R<sup>2</sup> computed between the two models.

405 mSCOPE allowed us to introduce a biochemical/optical heterogeneity in the vertical  
 406 dimension of simulated canopies. Additionally, we tested DART SIF simulation performance  
 407 when using the energy balance *eta* coefficients produced by mSCOPE. Comparison of total  
 408 nadir SIF<sub>TOC</sub> radiances produced by both models revealed almost the same results (Figure A3).  
 409 The indices of agreement were in all cases larger than 0.99, regardless exclusion or inclusion of  
 410 the mSCOPE *eta* coefficients in conducted simulations. The highest RMSE of just 0.221 W.m<sup>-2</sup>.  
 411 μm<sup>-1</sup>.sr<sup>-1</sup> and the lowest d = 0.9985 was found for simulation of 2-layered canopy with LAI =  
 412 2 and with the leaf energy balance included (Figure A3b).

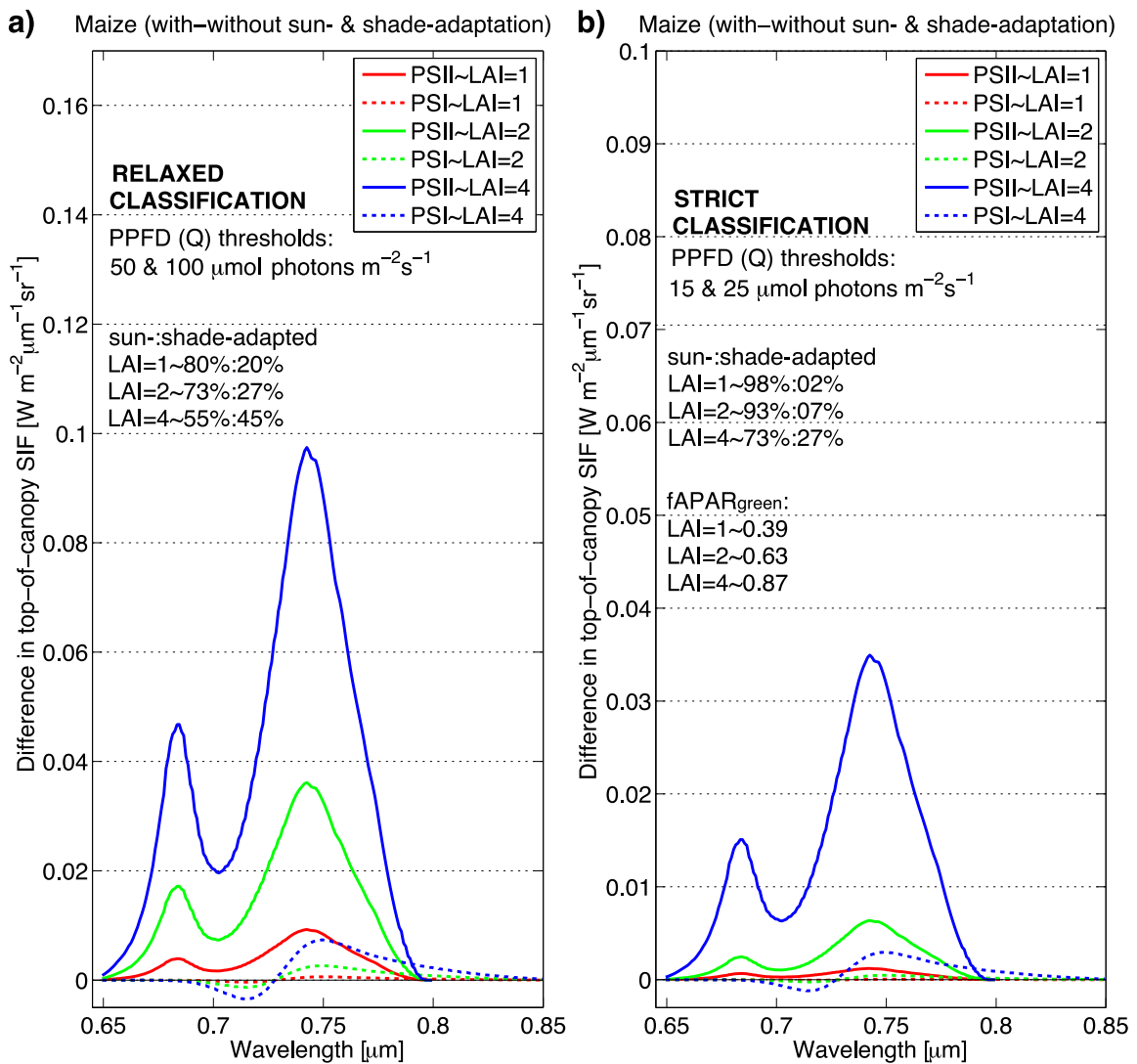
### 413 **3.2 Multi-angular comparison of DART and SCOPE canopy SIF simulations**

414 The similarity of DART and SCOPE SIF<sub>TOC</sub> simulations at 686 and 740 nm was also  
 415 investigated for viewing directions other than the nadir view. We compared values simulated  
 416 in the solar principal plane, with particular attention to the hotspot region, and computed  
 417 absolute differences between 27 DART and SCOPE turbid medium scenarios in all 212 viewing  
 418 directions. The smallest differences and the best agreement were found for SIF<sub>TOC</sub> at 686 nm,  
 419 Erectophile LAD and LAI = 1 (Figure A4), while the worse agreement and largest differences  
 420 were obtained for SIF<sub>TOC</sub> at 740 nm, Spherical LAD and LAI = 4 (Figure A5). Here, SCOPE  
 421 simulated slightly smaller SIF<sub>TOC</sub> values, except for VZA > 75°, where SIF<sub>TOC</sub> dropped  
 422 unexpectedly steeply down. Also, SCOPE values around the hotspot angles were about 1 W.m<sup>-2</sup>

## 2.1 VEGETATION SIMULATED AS FACETS

423  $^2 \cdot \mu\text{m}^{-1} \cdot \text{sr}^{-1}$  lower than the corresponding DART values. This is caused by differences in the  
 424 vegetation hotspot algorithms. SCOPE uses a Kuusk's analytical approximation, which does  
 425 not account for a bi-directional gap-fraction correlation with the canopy depth and consequently  
 426 underestimates the hotspot effect (Kallel and Nilson 2013), whereas hotspot in DART  
 427 simulations is physically modelled.

428 Analysis of multi-angular SIF differences among the three LADs stressed smaller  
 429 dissimilarities at 686 nm, having the best fit for the Spherical LAD, followed by the Erectophile  
 430 LAD, and then by the Planophile LAD. At 740 nm, the closest match occurred for the  
 431 Planophile LAD, while the Spherical and the Erectophile LADs showed equal discrepancies  
 432 (Figure A6). Nonetheless, the maximal absolute  $\text{SIF}_{\text{TOC}}$  difference between DART and SCOPE  
 433 oblique viewing directions of all scenarios was found to be  $< 0.8 \text{ W} \cdot \text{m}^{-2} \cdot \mu\text{m}^{-1} \cdot \text{sr}^{-1}$ .



434

435 Figure 4. Differences in DART top-of-canopy SIF radiance due to distinction of sun- and shade-adapted  
 436 leaves of regular maize canopies with LAI = 1, 2 and 4. Graphs illustrate two simulated scenarios of  
 437 photosynthetic photon flux density (PPFD or Q) classification thresholds: a) a ‘relaxed’ scenario with  
 438 high PPFD thresholds of 50 and 100  $\mu\text{mol.photons.m}^{-2}.\text{s}^{-1}$ , and b) a ‘strict’ scenario with low PPFD  
 439 thresholds of 10 and 25  $\mu\text{mol.photons.m}^{-2}.\text{s}^{-1}$ . For details about the double-threshold leaf light adaptation  
 440 classification see section 2.3.1.

### 441 3.3 Effect of sun- and shade-adapted maize foliage classification

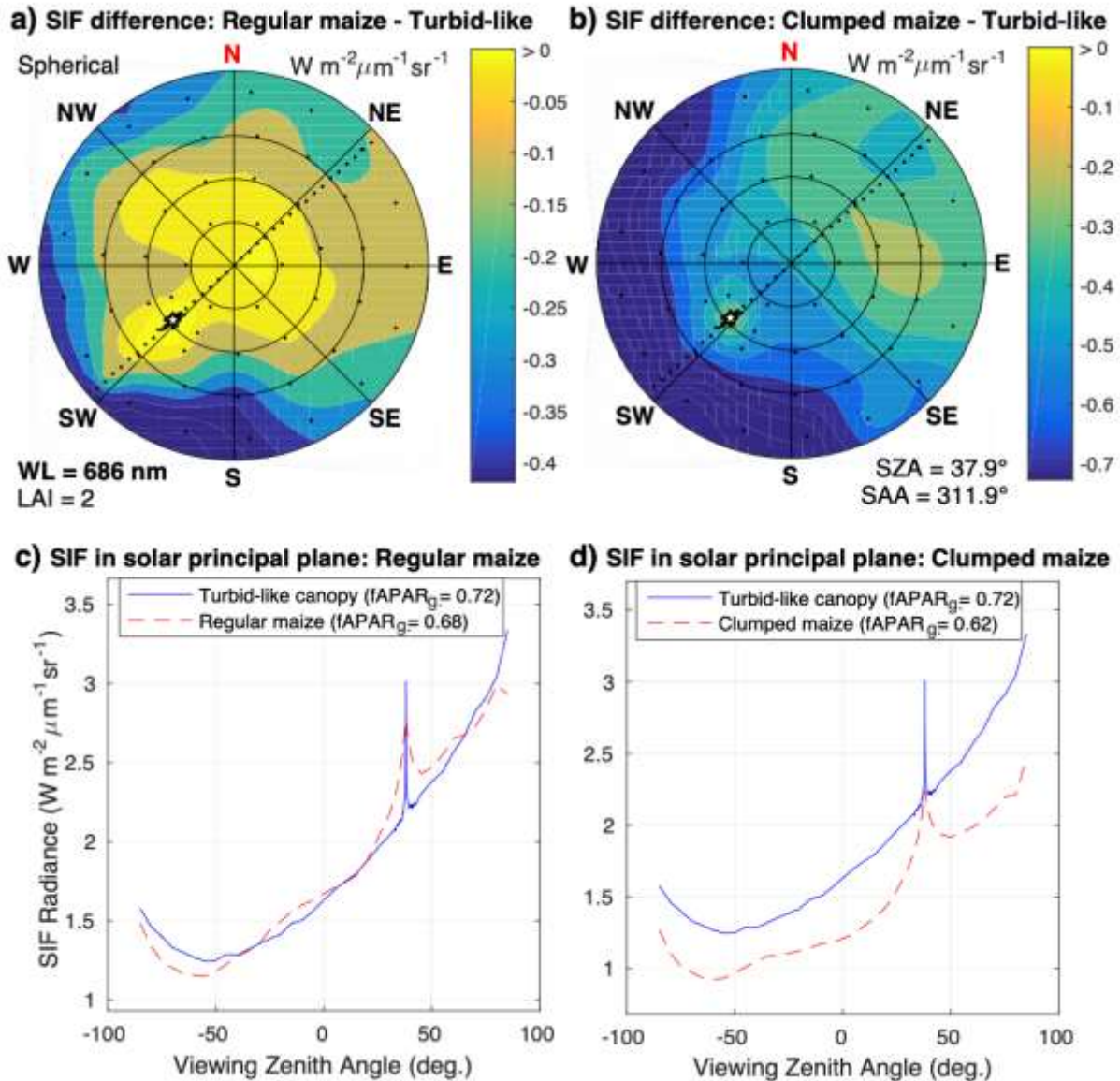
442 Two double-threshold classifications were used to assess the impact of sun- and shade-  
 443 adapted foliage differentiation on nadir PSI and PSII SIF<sub>TOC</sub> between 650-850 nm. The first  
 444 one, called ‘relaxed’, used the far-apart high Q thresholds (50 and 100  $\mu\text{mol.photons.m}^{-2}.\text{s}^{-1}$ ),  
 445 resulting in the sun-to-shade adapted foliage ratio ranging from 80:20% (LAI = 1) to 55:45%  
 446 (LAI = 4). Figure 4a shows that differences between SIF<sub>TOC</sub> signatures for simulations with and  
 447 without the differentiation of sun-/shade-adapted leaves were all positive for PSII, with the  
 448 highest value  $\approx 0.1 \text{ W.m}^{-2}.\mu\text{m}^{-1}.\text{sr}^{-1}$  around 740 nm for LAI = 4 ( $f\text{APAR}_{\text{green}} = 0.87$ ). Surprisingly,  
 449 the same differences for PSI between 700 and 725 nm were negative, demonstrating a greater  
 450 PSI SIF absorption by shade-adapted leaves having a higher chlorophyll *a+b* content of 75  
 451  $\mu\text{g.cm}^{-2}$ . Contrary to PSII SIF<sub>TOC</sub>, where *fqe* was increased from 0.016 to 0.022 for shade-  
 452 adapted leaves (Table 2), the constant PSI *fqe* of 0.002 could not compensate this increased  
 453 chlorophyll absorption. The second classification, called ‘strict’, used the closer and lower Q  
 454 thresholds (15 and 25  $\mu\text{mol.photons.m}^{-2}.\text{s}^{-1}$ ), resulting in canopies with a dominant portion of  
 455 sun-adapted leaves. The sun-to-shade adapted foliage ratio ranged from 98:2% (LAI = 1) to  
 456 73:27% (LAI = 4). Consequently, the SIF<sub>TOC</sub> differences were proportionally smaller (Figure  
 457 4b), with the largest value of 0.035  $\text{W.m}^{-2}.\mu\text{m}^{-1}.\text{sr}^{-1}$  for PSII SIF<sub>TOC</sub> at 740 nm (LAI = 4). PSI  
 458 SIF<sub>TOC</sub> differences were also reduced and remained negative between 700 and 725 nm.

### 459 3.4 Influence of foliage density and clumping in maize canopies

460 Figure 2 illustrates the impact of a leaf density increase (i.e., doubled LAI) and the  
 461 clumping of maize plants for LAI of 1 and 2. Nadir images of maize canopy SIF<sub>TOC</sub> at 740 nm  
 462 show the spatial dependence of SIF<sub>TOC</sub> radiance on the absorption of iPAR and on the  
 463 distribution of plant shadows. A linear increase of LAI triggered a non-linear and wavelength-  
 464 specific increase of SIF<sub>TOC</sub>. A bit more than 2-fold increase in far-red wavelengths from LAI =  
 465 1 to LAI = 4 corresponds to a similar increase in canopy  $f\text{APAR}_{\text{green}}$ , which is not the case for  
 466 the red SIF<sub>TOC</sub> nadir signal (Figure 2). The canopy clumping causes a decrease of SIF<sub>TOC</sub> at all

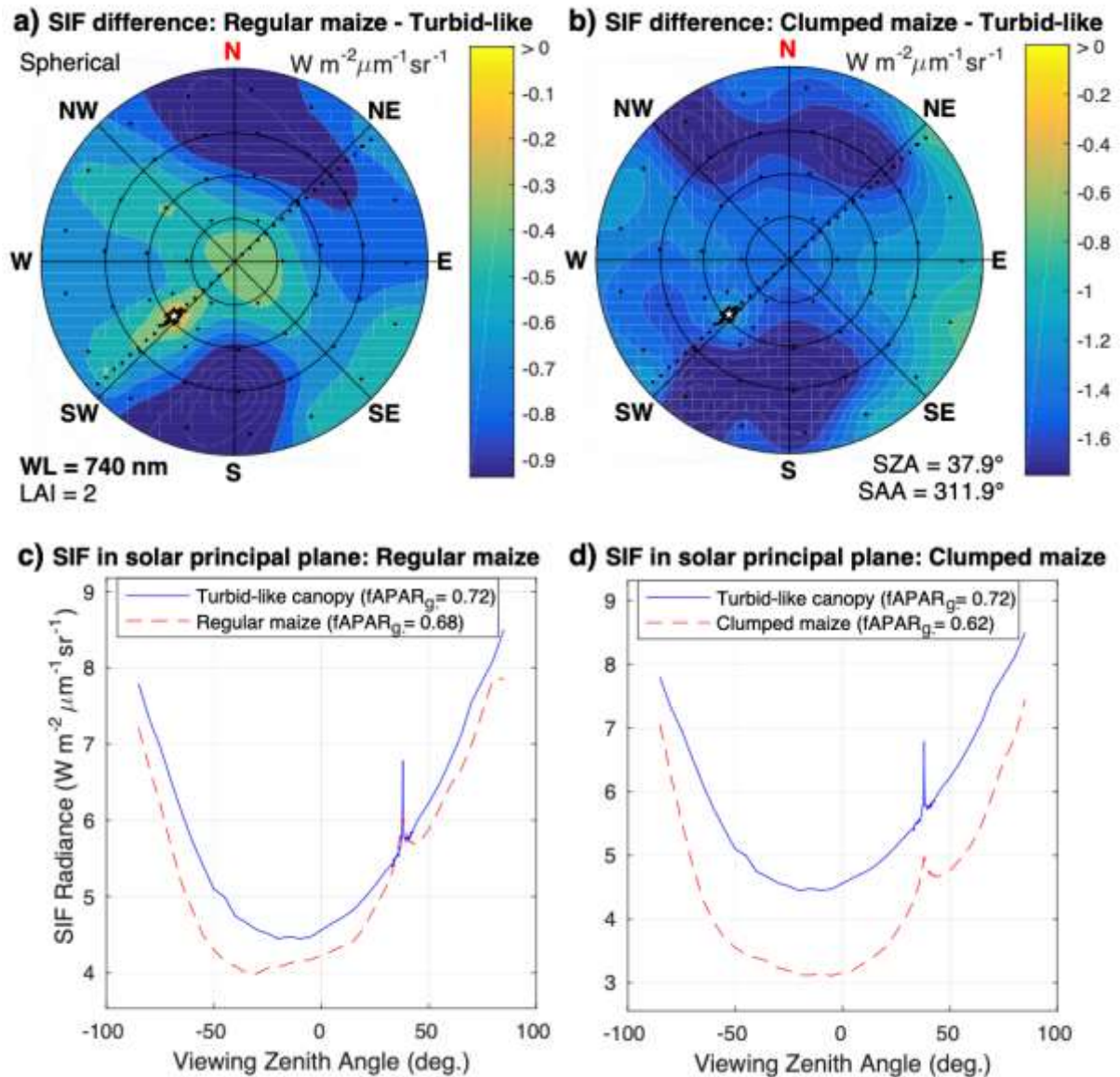
## 2.1 VEGETATION SIMULATED AS FACETS

467 wavelengths. The 50% decrease in CC caused SIF<sub>TOC</sub> reduction at 740 nm of about 0.4 for LAI  
 468 = 1 and 1.0  $W \cdot m^{-2} \cdot \mu m^{-1} \cdot sr^{-1}$  for LAI = 2, whereas reduction of LAI from 2 to 1 resulted in larger  
 469 SIF<sub>TOC</sub> declines of about 0.75 for CC = 50% and 1.6  $W \cdot m^{-2} \cdot \mu m^{-1} \cdot sr^{-1}$  for CC = 100%.



470

471 Figure 5. Multi-angular differences in SIF radiance at 686 nm between a) regular, b) clumped DART  
 472 3D maize canopies and a DART simulated turbid-like canopy with LAI = 2, Spherical LAD and loamy  
 473 soil as ground. SIF radiances in the solar principal plane for the turbid-like canopy together with the  
 474 regular (RMSE = 0.27 and d = 0.9) and the clumped (RMSE = 0.36 and d = 0.81) maize canopies are  
 475 illustrated in c) and d), respectively. Notations: the white star shows the solar position and black dots  
 476 indicate the simulated viewing directions; LAD ~ leaf angle distribution; LAI ~ leaf area index; WL ~  
 477 wavelength; SZA ~ solar zenith angle; SAA ~ solar azimuth angle; R<sup>2</sup> ~ coefficient of determination;  
 478 RMSE ~ root mean square error [ $W \cdot m^{-2} \cdot \mu m^{-1} \cdot sr^{-1}$ ]; d ~ index of agreement: 0 = no agreement, 1 = full  
 479 agreement.



480

481 Figure 6. Multi-angular differences in SIF radiance at 740 nm between a) regular, b) clumped DART  
 482 3D maize canopies and a DART simulated turbid-like canopy with LAI = 2, Spherical LAD and loamy  
 483 soil as ground. SIF radiances in the solar principal plane for the turbid-like canopy together with the  
 484 regular (RMSE = 0.42 and  $d = 0.92$ ) and the clumped (RMSE = 1.22 and  $d = 0.62$ ) maize canopies are  
 485 illustrated in c) and d), respectively (for abbreviations and symbols see Figure 5).

486 The interpretation of canopy architectural effects can be taken further by investigating the  
 487 multi-angular differences for  $SIF_{TOC}$  at 686 (Figure 5) and 740 nm (Figure 6), computed  
 488 between the turbid-like vegetation canopy, i.e., a random distribution of many small leaf facets  
 489 with the Spherical LAD, and the maize regular and clumped canopies of much larger leaves,  
 490 both with LAI = 2. DART simulated multi-angular  $SIF_{TOC}$  values of the turbid-like and regular  
 491 maize canopies at 686 nm are very close (RMSE = 0.27  $W.m^{-2}.\mu m^{-1}.sr^{-1}$ ,  $d = 0.9$ ) (see Figure

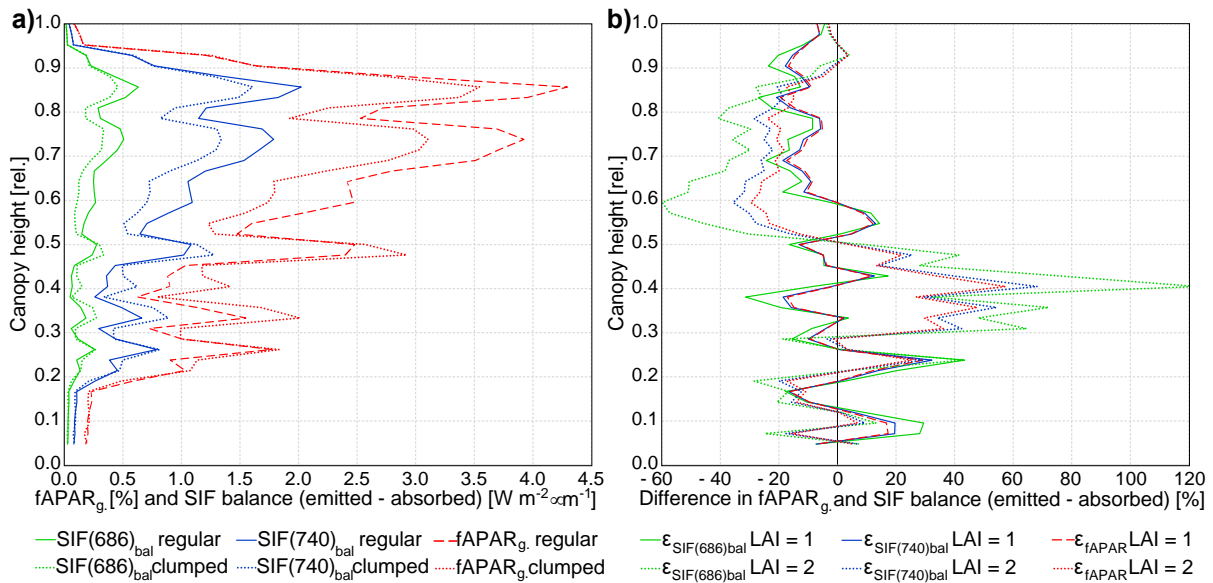


## 2.1 VEGETATION SIMULATED AS FACETS

492 5ac), indicating rather similar SIF absorptions within canopies and by soil. The maximum  
493 difference of just about  $-0.4 \text{ W.m}^{-2}.\mu\text{m}^{-1}.\text{sr}^{-1}$  appeared in very oblique viewing directions, in  
494 which maize plants scattered less SIF. Despite its slightly lower  $f\text{APAR}_{\text{green}}$  (0.68 vs. 0.72), the  
495 maize canopy scattered a bit more SIF in viewing directions around nadir and hotspot,  
496 producing a positive difference. This is caused by the maize geometrically explicit non-random  
497 LAD and large-sized leaf facets, redirecting the scattered SIF prevalingly in these directions.  
498 Larger size of maize leaves is decreasing scattering of photons, and consequently the diffuse  
499 fluxes, and causing a broader base of the  $\text{SIF}_{\text{TOC}}$  hotspot peak, observed when comparing the  
500 hotspots regions of maize and the turbid-like medium simulations. Although the multi-angular  
501 pattern for the clumped maize canopy looks also very similar ( $\text{RMSE} = 0.36 \text{ W.m}^{-2}.\mu\text{m}^{-1}.\text{sr}^{-1}$ ,  $d$   
502  $= 0.81$ ), the differences are all negative and significantly larger, with the maximum of about -  
503  $0.75 \text{ W.m}^{-2}.\mu\text{m}^{-1}.\text{sr}^{-1}$  (Figure 5bd). It means that the 50% foliage clumping increased scattering  
504 and the subsequent within-canopy absorption of SIF at 686 nm, because SIF absorption by the  
505 loamy soil beneath the clumped canopy was 7% lower than in the regular canopy, i.e., unable  
506 to cause the  $\text{SIF}_{\text{TOC}}$  reduction. The angular distributions of the same differences at 740 nm look  
507 different (Figure 6), as they are ruled mainly by scattering related to the canopy architecture.  
508 The decrease in intensity of maize far-red  $\text{SIF}_{\text{TOC}}$  is driven by the species-specific foliage  
509 distribution and geometry, significantly larger maize leaf size combined with a high leaf single  
510 scattering albedo at 740 nm and the soil absorption.  $\text{SIF}_{\text{TOC}}$  differences in Figure 6 are negative  
511 for both regular ( $\text{RMSE} = 0.42 \text{ W.m}^{-2}.\mu\text{m}^{-1}.\text{sr}^{-1}$ ,  $d = 0.92$ ) and clumped canopy of  $\text{LAI} = 2$ , but  
512 larger for the latter one ( $\text{RMSE} = 1.22 \text{ W.m}^{-2}.\mu\text{m}^{-1}.\text{sr}^{-1}$ ,  $d = 0.62$ ). Results of DART radiative  
513 budget revealed that the introduction of clumping did not increase but lowered (by 12%) the  
514 amount of soil intercepted and absorbed SIF. Hence, it is not soil but clumping-induced within  
515 canopy SIF optical interactions that are responsible for this extra reduction of  $\text{SIF}_{\text{TOC}}$ .

516 The relative contribution from different canopy parts (horizontal layers) to  $\text{SIF}_{\text{TOC}}$  and its  
517 modulation by  $f\text{APAR}_{\text{green}}$  or by SIF scattering and absorption can be investigated by plotting  
518 vertical canopy height profiles of  $f\text{APAR}_{\text{green}}$  together with corresponding SIF balances of both  
519 fluorescence wavelengths. Figure 7a shows that SIF balances are positive at all heights, i.e.,  
520 every layer act as a SIF source, and they follow, in general, changes in  $f\text{APAR}_{\text{green}}$ . The foliage  
521 clumping decreased significantly  $f\text{APAR}_{\text{green}}$ ,  $\text{SIF}(\lambda)_{\text{bal}}$  and also  $\text{SIF}_{\text{omni}}(\lambda)_{\text{esc}}$  (not shown) in  
522 the upper half of the canopy with  $\text{LAI} = 2$ , causing the overall reduction of  $\text{SIF}_{\text{TOC}}$ , but it

523 increased all of them in canopy parts below. It means that the lower leaves of the clumped  
 524 canopy contributed to the simulated SIF<sub>TOC</sub> more than the same leaves of the regular canopy.



525  
 526 Figure 7. Vertical profiles of a)  $fAPAR_{green}$ , SIF balances (for maize canopies of LAI = 2) and b)  
 527 their relative differences at 686 and 740 nm computed between regularly spaced and clumped  
 528 canopies of the same LAI (for LAI = 1 and 2). Each 2.5 cm thick canopy layer is presented as a  
 529 point of the relative canopy height [0-1]. For details about computations of  $fAPAR_{green}$ , SIF  
 530 balance ( $SIF(\lambda)_{bal}$ ) and their relative differences ( $\epsilon_{fAPAR(\lambda)}$  and  $\epsilon_{SIF(\lambda)_{bal}}$ ) see section 2.4.

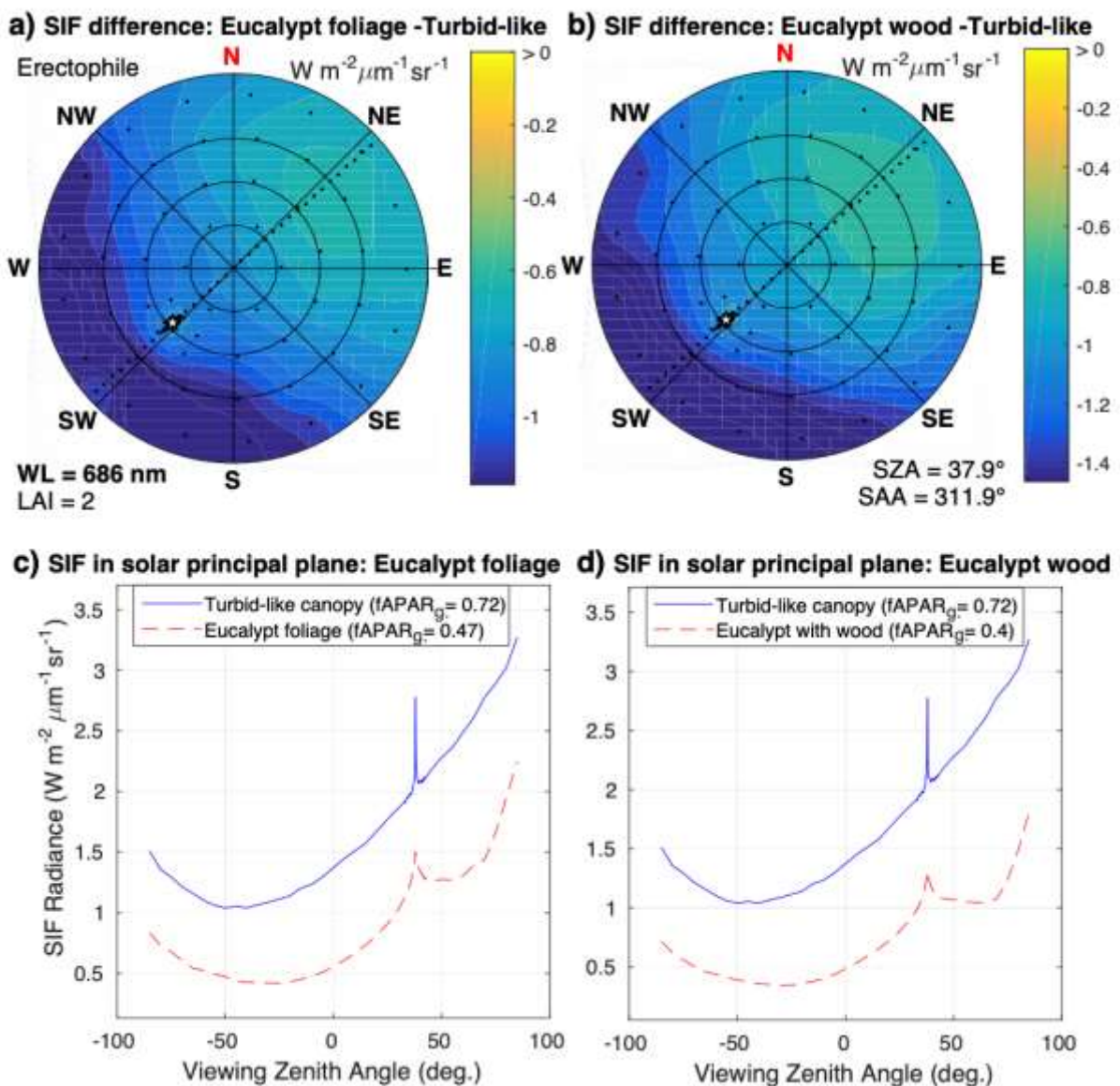
531 Figure 7b, depicting the  $fAPAR_{green}$  and  $SIF(\lambda)_{bal}$  relative differences between the regular  
 532 and clumped canopies, provides a further insight in this behaviour and dependencies between  
 533 SIF and  $fAPAR_{green}$  radiative budgets. It illustrates a clumping-induced steady reduction of  
 534  $fAPAR_{green}$  and SIF balance differences in upper 40% of the canopy with LAI = 1, whereas the  
 535 differences in lower 60% fluctuate between positive and negative values.  $\epsilon_{SIF(740)_{bal}}$  for  
 536 LAI = 1 follows quite closely  $\epsilon_{fAPAR(\lambda)}$ , suggesting that variability of SIF fluxes at 740 nm is  
 537 ruled mainly by clumping-induced changes in distribution of shadows and sun flecks, while  
 538  $\epsilon_{SIF(686)_{bal}}$  shows a bit more negative or positive deviations from  $\epsilon_{fAPAR(\lambda)}$ , caused by a local  
 539 increase or decrease in chlorophyll absorption of SIF at 686 nm. SIF<sub>TOC</sub> for LAI = 2 is formed  
 540 by steady but greater negative differences in the canopy top half that are partially balanced out  
 541 by nearly 2-fold larger positive differences between 30 and 50% of the canopy relative height.  
 542 Comparable differences for both LAI cases between the bottom and 30% of the canopy height  
 543 indicate very similar  $fAPAR_{green}$  and SIF radiative budgets, driven by mostly diffused low-  
 544 intensity PAR. The negative  $\epsilon_{fAPAR(\lambda)}$  and  $\epsilon_{SIF(\lambda)_{bal}}$  values in the upper half of the canopy are



## 2.1 VEGETATION SIMULATED AS FACETS

545 caused by combination of higher (doubled) LAI with foliage clumping that increased internal  
 546 shadowing and consequently reduced  $fAPAR_{green}$ . It also enhanced a number of SIF photons  
 547 interacting with leaf facets, resulting in a higher fluorescence absorption, especially at 686 nm.  
 548 Scientifically interesting is the opposite behaviour between 30 and 50% of the canopy height,  
 549 where it boosted  $fAPAR_{green}$  and consequently SIF emissions, but simultaneously diminished  
 550 SIF absorption, which is evidenced by  $\epsilon_{SIF(686)_{bal}}$  and  $\epsilon_{SIF(740)_{bal}} > \epsilon_{fAPAR(\lambda)}$ . The total energy  
 551 released from these positive  $SIF(\lambda)_{bal}$  differences was, nevertheless, unable to fully compensate  
 552 the negative  $SIF(\lambda)_{bal}$  differences induced by clumping in the upper canopy parts (Figure 7a).

### 553 3.5 Impacts of foliage clumping and wood of white peppermint trees

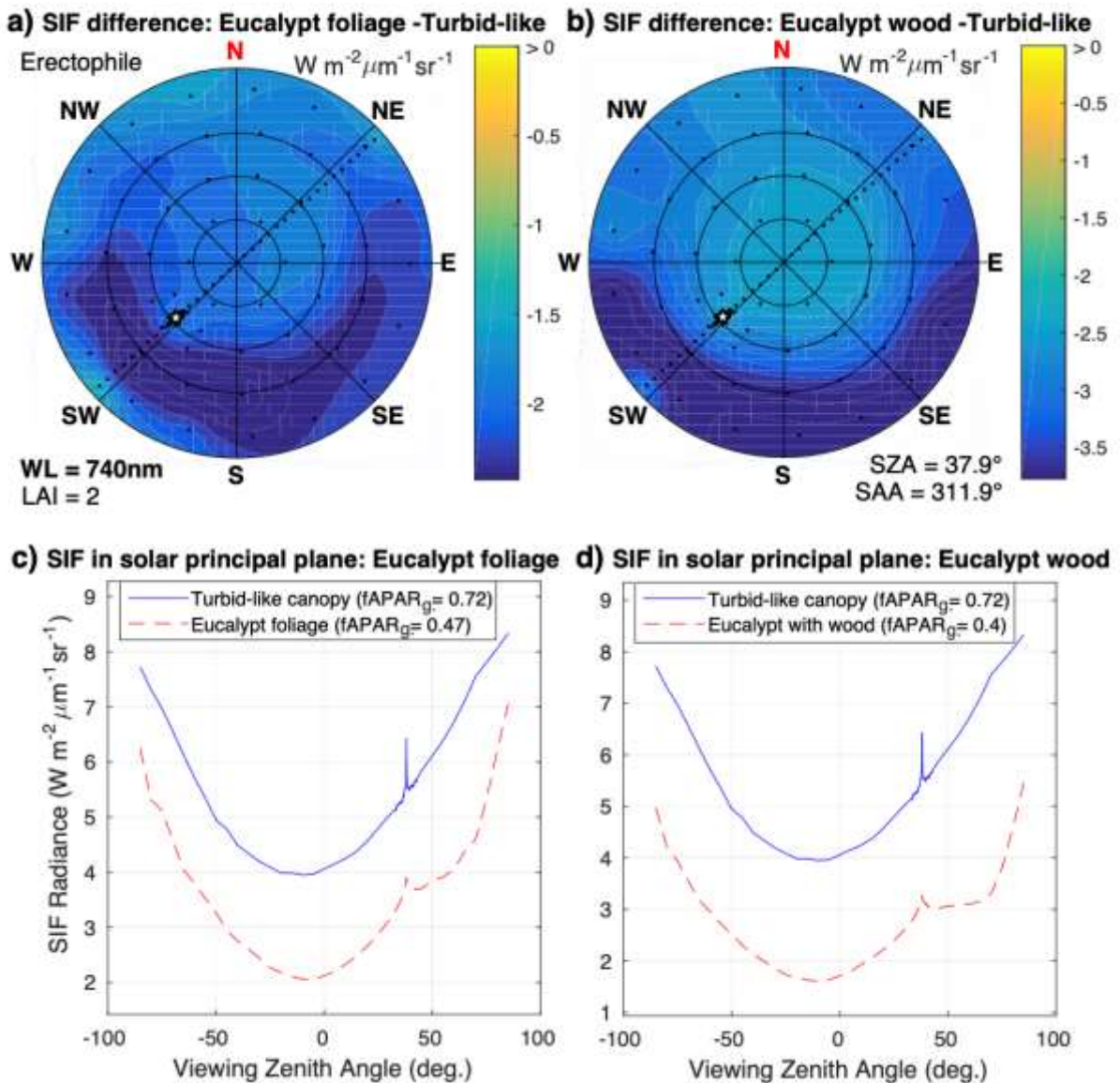


554

555 Figure 8. Multi-angular differences in SIF radiance at 686 nm between a) a dense eucalyptus canopy  
556 created only by foliage, b) the same canopy containing also woody components and a DART simulated  
557 turbid-like canopy, all with LAI = 2, Erectophile LAD and loamy soil as ground. SIF radiances in the  
558 solar principal plane for the turbid-like canopy together with the foliage-only (RMSE = 0.82 and  $d =$   
559 0.55) and the foliage with wood (RMSE = 1.0 and  $d = 0.47$ ) eucalypt canopies are illustrated in c) and  
560 d), respectively (for abbreviations and symbols see Figure 5).

561 DART 3D modelling allowed us to investigate previously unquantified impacts of foliage  
562 structure and woody material on  $fAPAR_{green}$  and on optical interactions of SIF photons inside  
563 white peppermint canopies. Figure 3 shows nadir PSII SIF<sub>TOC</sub> images at 740 nm for dense  
564 eucalyptus forest canopies without and with presence of the woody parts. A simple visual  
565 comparison of the two images reveals a lower SIF<sub>TOC</sub> in the lower right corner of the image  
566 caused by a deeper shadowing after inclusion of trunks and branches. One can also detect  
567 several large non-fluorescing branches in the SIF<sub>TOC</sub> image, visible due to a strong reflection  
568 of far-red SIF photons by peppermint bark ( $\rho_{740\text{ nm}} \approx 50\%$ ).

## 2.1 VEGETATION SIMULATED AS FACETS



569

570 Figure 9. Multi-angular differences in SIF radiance at 740 nm between a) a dense eucalyptus canopy  
 571 created only by foliage, b) the same canopy containing also woody components and a DART simulated  
 572 turbid-like canopy, all with LAI = 2, Erectophile LAD and loamy soil as ground. SIF radiances in the  
 573 solar principal plane for the turbid-like canopy together with the foliage-only (RMSE = 1.93 and d =  
 574 0.47) and the foliage with wood (RMSE = 2.68 and d = 0.35) eucalypt canopies are illustrated in c) and  
 575 d), respectively (for abbreviations and symbols see Figure 5).

576 In comparison with the multi-directional SIF radiance of the turbid-like canopy, the dense  
 577 eucalyptus stand without wood showed statistically significant decreases in  $SIF_{TOC}$  at 686 nm  
 578 (RMSE =  $0.82 W \cdot m^{-2} \cdot \mu m^{-1} \cdot sr^{-1}$ ,  $d = 0.55$ ) (Figure 8ac) and even greater at 740 nm (RMSE =  
 579  $1.93 W \cdot m^{-2} \cdot \mu m^{-1} \cdot sr^{-1}$ ,  $d = 0.47$ ) (Figure 9ac). This drop, reaching up to  $-1.2 W \cdot m^{-2} \cdot \mu m^{-1} \cdot sr^{-1}$  and  
 580 almost  $-2.5 W \cdot m^{-2} \cdot \mu m^{-1} \cdot sr^{-1}$ , respectively, can be explained by the Erectophile LAD of the  
 581 small-sized narrow white peppermint leaves, and by their strong and spatially irregular

582 clumping at the branch level. Presence of woody structures did not change considerably the  
 583 angular patterns of the SIF<sub>TOC</sub> differences, but caused its further suppression at 686 nm (RMSE  
 584 = 1.0 W.m<sup>-2</sup>. μm<sup>-1</sup>.sr<sup>-1</sup>, d = 0.47) (Figure 8bd) and even larger differences at 740 nm (RMSE =  
 585 2.68 W.m<sup>-2</sup>. μm<sup>-1</sup>.sr<sup>-1</sup>, d = 0.35) (Figure 9bd). Interestingly, it deepened the shape the solar  
 586 principal plane SIF<sub>TOC</sub> curve in back-scattering oblique viewing directions behind the hotspot  
 587 region, producing the maximum difference of almost -1.4 W.m<sup>-2</sup>. μm<sup>-1</sup>.sr<sup>-1</sup> at 686 nm and  
 588 around -3.7 W.m<sup>-2</sup>. μm<sup>-1</sup>.sr<sup>-1</sup> at 740 nm.

589 The DART ability to simulate forest stands with and without woody elements opened an  
 590 opportunity for quantification of their potential impacts on SIF emitted, observed and escaped  
 591 in the nadir direction from white peppermint dense and sparse canopies (Table 2). We  
 592 quantified the wood shading effect, causing changes in canopy fAPAR<sub>green</sub> due to the scattering  
 593 and absorption of iPAR, and the obstruction (blocking) effect of eucalyptus wood, caused by  
 594 scattering and absorption of SIF photons by bark. As expected, wood shadowing lowered SIF  
 595 emitted at both investigated wavelengths by the percentage equal to the fAPAR<sub>green</sub> reduction,  
 596 i.e., by 17.0% for the dense and 9.7% for the sparse canopy. Comparison of the foliage only  
 597 SIF<sub>TOC</sub> with the foliage and wood SIF<sub>TOC</sub> revealed lesser impacts at 686 nm than at 740 nm.  
 598 SIF escape probability factors of the simulated eucalyptus canopies were generally low:  
 599 SIF<sub>nadir(686)</sub><sub>esc</sub> ≤ 0.15 and SIF<sub>nadir(740)</sub><sub>esc</sub> ≤ 0.27. Overall, the wood obstruction effect was  
 600 greater on far-red than red SIF escape factors, causing a consistent decrease of 4-6% in  
 601 SIF<sub>nadir(740)</sub><sub>esc</sub>, but almost no change in SIF<sub>nadir(686)</sub><sub>esc</sub> for the sparse and less than 2%  
 602 increase for the dense canopy (Table 2).

603

604 Table 2. DART simulated impacts of woody material and bark on fAPAR<sub>green</sub> of leaves, SIF leaf  
 605 emissions, nadir top-of-canopy SIF<sub>TOC</sub> and nadir SIF escape probability factor at 686 and 740 nm of two  
 606 white peppermint (*Eucalyptus pulchella*) stands with dense and sparse canopy covers (CC) and LAI =  
 607 2.5. The relative impact on canopy SIF emitted by leaves (Bold fonts), is caused either by shadows  
 608 casted on photosynthetically active foliage (*shading effect*; Eq. 8) or by absorption and scattering of SIF  
 609 photons by bark-covered wood in combination with green foliage (*obstruction effect*; Eq. 11); (↓)  
 610 indicates a decreasing and (↑) an increasing effect.

DART scenario	Dense canopy (CC ≈ 80%)			Sparse canopy (CC ≈ 40%)		
	Foliage only	Foliage & Wood	<b>Relative impact [%]</b>	Foliage only	Foliage & Wood	<b>Relative impact [%]</b>
fAPAR <sub>green</sub> of leaves	0.466	0.399		0.306	0.279	

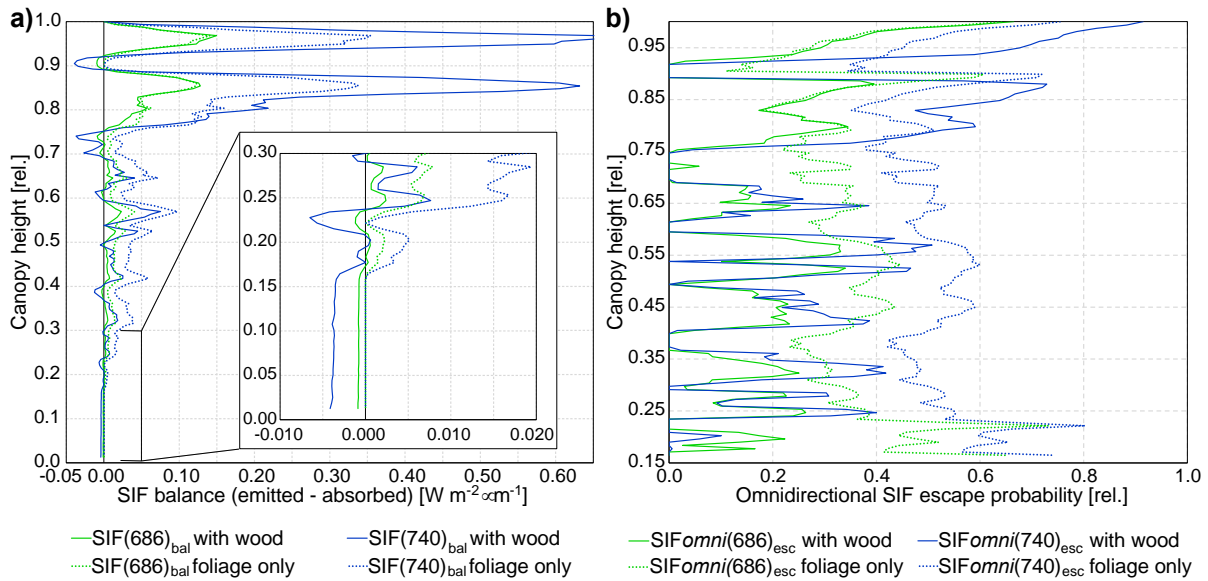
## 2.1 VEGETATION SIMULATED AS FACETS

<i>Shading effect</i> ( $\varepsilon_{\text{fAPAR}(400-750)}$ )			<b>17.0</b> (↓)		<b>9.7</b> (↓)	
<u>Red SIF (686 nm)</u>						
Emitted by leaves [ $\text{W}\cdot\text{m}^{-2}\cdot\mu\text{m}^{-1}$ ]	11.626	9.939	7.618	6.945		
Nadir $\text{SIF}_{\text{TOC}}$ [ $\text{W}\cdot\text{m}^{-2}\cdot\mu\text{m}^{-1}\cdot\text{sr}^{-1}$ ]	0.554	0.481	0.303	0.275		
$\text{SIF}_{\text{nadir}(686)}_{\text{esc}}$ [rel.]	0.150	0.152	0.125	0.124		
<i>Obstruction effect</i> ( $\varepsilon_{\text{SIF}(686)}_{\text{esc}}$ )			<b>-1.5</b> (↑)		<b>0.6</b> (↓)	
<u>Far-red SIF (740 nm)</u>						
Emitted by leaves [ $\text{W}\cdot\text{m}^{-2}\cdot\mu\text{m}^{-1}$ ]	24.461	20.914	16.029	14.613		
Nadir $\text{SIF}_{\text{TOC}}$ [ $\text{W}\cdot\text{m}^{-2}\cdot\mu\text{m}^{-1}\cdot\text{sr}^{-1}$ ]	2.093	1.693	1.260	1.108		
$\text{SIF}_{\text{nadir}(740)}_{\text{esc}}$ [rel.]	0.269	0.254	0.247	0.238		
<i>Obstruction effect</i> ( $\varepsilon_{\text{SIF}(740)}_{\text{esc}}$ )			<b>5.7</b> (↓)		<b>3.6</b> (↓)	

611

612 More detailed understanding of the wood-induced effects inside the dense white  
613 peppermint canopy can be obtained from analysing its DART-simulated vertical profiles of SIF  
614 balances and omnidirectional SIF escape factors. Plots of  $\text{SIF}(\lambda)_{\text{bal}}$  in Figure 10a and  
615  $\text{SIF}_{\text{omni}}(\lambda)_{\text{esc}}$  in Figure 10b, shown across the relative stand height, revealed two significant  
616 findings. First, every leaf-containing part of the canopy comprised of only foliage is acting as  
617 a SIF source ( $\text{SIF}_{\text{omni}}(\lambda)_{\text{esc}} > 0$ ), but the presence of woody components turned the parts  
618 emitting only a little fluorescence into SIF sinks ( $\text{SIF}_{\text{omni}}(\lambda)_{\text{esc}} = 0$ ). Second, a majority of the  
619  $\text{SIF}_{\text{TOC}}$  signal originates from leaves occupying top 25% percent of the eucalyptus canopy  
620 height. Although the close-up of the 0-30% canopy height section in Figure 10a shows a strong  
621 SIF absorption by trunks and lower branches that results in  $\text{SIF}(\lambda)_{\text{bal}} < 0$  (especially at 740 nm),  
622 different SIF energy budget results were obtained for top 25% (i.e., 75-100%) of the canopy.  
623 The wood presence in this highly emitting canopy part increased the  $\text{SIF}(686)_{\text{bal}}$  values only  
624 negligibly, as the bark and photosynthesizing leaves were capable of absorbing nearly all extra  
625 SIF photons reflected at 686 nm by woody structures. This result is in line with a very slight  
626 increase of  $\text{SIF}_{\text{nadir}}(686)_{\text{esc}}$  listed in Table 2. Wood presence, however, decreased absorptance  
627 and increased more than 2-fold reflectance of SIF at 740 nm, which significantly enhanced  
628 (almost doubled) the  $\text{SIF}(740)_{\text{bal}}$  values in this upper canopy part. Despite this limited local  
629 boost, wood obstructions suppressed values of both  $\text{SIF}(740)_{\text{bal}}$  and  $\text{SIF}_{\text{omni}}(740)_{\text{esc}}$  in the rest

630 of the canopy profile, leading to an overall 5.7% reduction in canopy  $SIF_{nadir}(740)_{esc}$   
 631 (Table 2) and, consequently, in a decrease of multi-angular  $SIF_{TOC}$  (Figure 9ab).



633 Figure 10. Vertical profiles of a) SIF balances ( $SIF(\lambda)_{bal}$ ) and b) relative omnidirectional SIF  
 634 escape factors ( $SIF_{omni}(\lambda)_{esc}$ ) at 686 and 740 nm for a dense white peppermint (*Eucalyptus*  
 635 *pulchella*) canopy ( $CC \approx 80\%$  and  $LAI = 2$ ) created only by foliage (dashed lines) and the same  
 636 canopy containing also woody components (solid lines). Each 10 cm thick canopy layer is  
 637 presented as a point of the relative canopy height [0-1]. For details about computations of  $SIF(\lambda)_{bal}$   
 638 and  $SIF_{omni}(\lambda)_{esc}$  see section 2.4.

640 **4. Discussion**

641 **4.1 Comparison of DART and SCOPE/mSCOPE models**

642 DART outputs were nearly in a perfect agreement with the corresponding results obtained  
 643 for simple, turbid medium vegetation scenes with SCOPE and mSCOPE. Better agreements  
 644 were obtained for the  $SIF_{TOC}$  local maximum at 686 nm, where the signal is attenuated by the  
 645 SIF chlorophyll absorption. Since the  $SIF_{TOC}$  values at 740 nm are controlled dominantly by  
 646 canopy structural traits, the smallest discrepancies were obtained for the geometrically more  
 647 uniform Planophile LAD. Here, the  $SIF_{TOC}$  signal is dominated by the first order scattering of  
 648 prevalingly horizontally oriented leaves, lowering the occurrence of fluorescence absorption.  
 649 The largest multi-angular  $SIF_{TOC}$  differences in all tested LAD and LAI scenarios occurred in  
 650 very oblique viewing angles, in which the modelled radiance is impacted by uncertainties in  
 651 angular discretization of the upper hemisphere.

## 2.1 VEGETATION SIMULATED AS FACETS

652 Despite of a generally high agreement with SCOPE/mSCOPE simulations, this model cross  
653 comparison is not a fully sufficient replacement of an independent validation of the DART  
654 model, which is expected to be performed with real canopy SIF<sub>TOC</sub> measurements in a near  
655 future. Nonetheless, this comparison provides the evidence that current integration of the  
656 Fluspect model and implementation of the 3D flux-tracking radiative transfer of SIF emitted  
657 from geometrically explicit leaves are as plausible as already validated 1D radiative transfer  
658 modelling approaches of SCOPE and mSCOPE models (Migliavacca et al. 2017; Pacheco-  
659 Labrador et al. 2019; van der Tol et al. 2016; Vilfan et al. 2019). This conclusion provides us  
660 with a high level of confidence that the radiative transfer modelling of SIF in DART can be  
661 used to investigate the major canopy structural controls of SIF<sub>TOC</sub> in geometrically explicit 3D  
662 canopies, which structural complexity cannot be represented and tested in SCOPE or mSCOPE.

### 663 **4.2 SIF changes due to classification of sun-/shade-adapted leaves and canopy structure**

664 Distinct parametrization of sun- and shade-adapted leaves did not result in major  
665 differences in SIF<sub>TOC</sub>, but other canopy structural parameters were found to be more important.  
666 The specific distinction of leaf *fqe* for sun- and shade-adapted foliage appeared to have a smaller  
667 impact on DART simulated nadir SIF<sub>TOC</sub> than increasing LAI and foliage clumping reducing  
668 CC from 100% to 50% (c.f., Figure 1 and Figure 3). Yet, the impact of the leaf-light adaptation  
669 effect might increase, if a DART user applies Q double-threshold values that favour strongly  
670 the shade- over the sun-adapted class and simultaneously increases the PSI and PSII *fqe* inputs.  
671 Secondly, the influence of the shade-adapted class would be more significant when tested for  
672 naturally more clumped and taller (e.g., forest) canopies. Therefore, identification of correct Q  
673 thresholds and sun/shade *fqe* values are, together with measurements of canopy gaps and foliage  
674 clumping, essential for further investigation of the photosynthetic light adaptations and their  
675 impacts on SIF<sub>TOC</sub>.

676 When evaluating impacts of maize canopy structural traits, our nadir SIF<sub>TOC</sub> results  
677 indicated a general superior role of LAI over the foliage clumping. However, doubling the  
678 foliage clumping of maize crop with LAI = 2 caused such a strong increase in absorption of red  
679 SIF photons by chlorophylls that diminished and fully equalled the previous increase in SIF<sub>TOC</sub>  
680 between 650 and 725 nm caused by doubling the number of regularly spaced plants, i.e., twice  
681 higher LAI (Figure 2). Interpretation of DART 3D radiative budget computed for the two SIF  
682 local maximums informed us that this strong red SIF reduction took place in the upper half of



683 the canopy (specifically between 50 and 90% of the canopy height; Figure 7), because the  
 684 clumping caused a slight enhancement of SIF energy fluxes in most of the lower half canopy  
 685 parts and the absorption of SIF by soil background was after the clumping introduction lowered.  
 686 The fact that relative differences of red SIF balances in upper halves of the clumped and  
 687 unclumped canopies are 2-fold more negative than the same differences of  $fAPAR_{green}$  (Figure  
 688 7b) indicates that the increase in foliage shadowing is responsible only for a half of this  
 689 clumping-induced SIF reduction. The second half is caused by a more frequent recollision and  
 690 consequent greater absorption of red SIF photons by leaf photosynthetic pigments. Clumping  
 691 driven results for  $LAI = 1$  showed less consistent and milder effects, which means that canopy  
 692 must have a certain minimal leaf density to produce these interactions.

693 Clumping impacts caused by decreasing CC can be also demonstrated on the example of  
 694 white peppermint stands without woody material. According to results listed in Table 2,  
 695 decrease of CC from 80% to 40% triggered a reduction in  $fAPAR_{green}$  and, consequently, in  
 696 emitted SIF by 34%, and simultaneously lowered the  $SIF_{TOC}$  by 45% at 686 nm and by 40% at  
 697 740 nm. Thereby, if one accepts an assumption that scattering rates of red and far-red SIF  
 698 photons by the canopy structures (including structures of a leaf interior without foliar pigments)  
 699 are equal, then doubling the leaf density while keeping a constant canopy  $LAI = 2$  induced an  
 700 additional 5% decrease in red  $SIF_{TOC}$  attributed to a higher red SIF absorption by chlorophylls.  
 701 It is important to mention that different quantitative impacts of LAI and foliage clumping on  
 702  $SIF_{TOC}$  might be revealed if the classification of sun-/shade-adapted leaves is included and  
 703 different (i.e., light adaptation specific) PSI and PSII  $fqe$  values are specified by a DART user.  
 704 Since the natural variability in  $fqe$  and leaf biochemistry was not accounted for in this study, a  
 705 direct comparison (validation) of these results with SIF observations of real croplands or forests  
 706 (e.g., Guan et al. 2015; He et al. 2020; Peng et al. 2020; Wang et al. 2020) would be misleading.

707 Multi-angular DART simulations of  $SIF_{TOC}$  demonstrate that the influence of leaf size,  
 708 foliage angularity and its clumping (CC) is equally or even more crucial for modulating  $SIF_{TOC}$   
 709 in oblique viewing directions. The polar plots of  $SIF_{TOC}$  at 686 nm for maize (Figure 5b) and  
 710 eucalyptus (Figure 8a) canopies with  $LAI = 2$  revealed the largest influence in very oblique  
 711 backward directions behind the hotspot and the smallest impact in forward directions opposite  
 712 to the hotspot. The patterns of angular anisotropy for  $SIF_{TOC}$  at 740 nm are rather different. A  
 713 significant impact of maize canopy structure was found around the Northern and the Southern



## 2.1 VEGETATION SIMULATED AS FACETS

714 viewing angles (Figure 6b), whereas only the Southern viewing directions were impacted by  
715 the eucalyptus canopy architecture (Figure 9a). Thus, far-red  $SIF_{TOC}$  of each architecturally  
716 distinct plant formation (i.e., plant functional type) must be approached individually and the  
717 canopy specific structural confounding effects must be removed or at least reduced before any  
718 application of remotely sensed  $SIF_{TOC}$ . This recommendation is in line with a number of recent  
719 works developing far-red  $SIF_{TOC}$  normalization approaches to mitigate the canopy structural  
720 effects (Liu et al. 2019b; Yang and van der Tol 2018; Yang et al. 2020b; Zeng et al. 2019).

### 721 **4.3 Impacts of wood structures on eucalyptus $SIF_{TOC}$ signal and $SIF$ escape factors**

722 Accounting for presence of bark-covered wood structures in our eucalyptus simulations  
723 decreased nadir 740 nm  $SIF_{TOC}$  by about 23% for the dense canopy and by 13% for the sparse  
724 canopy (Table 2). Results suggest that approximately one quarter of the total  $SIF$  reduction is  
725 caused by direct optical interactions (obstruction) of far-red  $SIF$  photons with bark surfaces in  
726 combination with green leaves under the natural geometrical distributions, whereas three  
727 quarters of the reduction resulted from the reduction in  $APAR_{green}$  due to wood shadowing.  
728 Having the bark reflectance and absorptance at 740 nm both equal to 50%, the wood structures  
729 of white peppermint trees acted, on one hand, as strong reflectors and boosted the far-red  $SIF$   
730 emission produced in top 25% of the dense canopy (Figure 10a). On the other hand, they acted  
731 as a far-red  $SIF$  sink in the rest of the canopy, i.e., in lower 75% of the canopy relative height.  
732 Although it is expected that tree species with a lower bark near infrared reflectance will  
733 demonstrate radiative budgets with a higher far-red  $SIF$  obstruction (absorptance), the  
734 consistently decreasing nadir obstruction effects of both modelled eucalyptus stand indicate that  
735 the wood obstruction is a regular confounding factor that must be treated as a systematic error  
736 source. Therefore, it should be accounted for, or if feasible even corrected, when interpreting  
737 far-red  $SIF_{TOC}$  data sensed remotely over forests.

738 The effect of woody material on nadir  $SIF_{TOC}$  at 686 nm was smaller, because the total pool  
739 of canopy red  $SIF$  photons originating just from PSII is naturally small and additionally reduced  
740 by absorption of photosynthetic pigments. Interestingly, the bark absorptance of 60% and  
741 reflectance of 40% at 686 nm, in combination with the specific geometry of eucalypt tree  
742 crowns (i.e., a strong branch foliage clumping with Erectophile LAD), decreased the red  $SIF$   
743 nadir escape factor of the sparse canopy by 0.6%, whereas the same  $SIF$  escape factor in the  
744 dense canopy was increased by 1.5%. If we accept these simulations as generally applicable,

745 we may conclude that the presence of wood affects the red SIF forest canopy balance in both  
 746 negative and positive ways. However, the impact is generally small, predominantly influencing  
 747 the less emitting lower 75% of the canopy height rather than larger emissions originating from  
 748 top 25% of the canopy. Since we modelled and analysed only two mono-species eucalyptus  
 749 stands, additional simulations for other tree species, including natural variability in species-  
 750 specific optical, biochemical and structural properties, will be essential to draw more  
 751 comprehensive and generic conclusions regarding the wood obstruction effects.

752 DART estimates of the relative eucalyptus canopy SIF escape factor in the nadir direction,  
 753 which can be used to compute the apparent SIF efficiency (a gross primary production proxy  
 754 less impacted by canopy structures; Wang et al. 2020), were quite low, smaller than 0.15 for  
 755 red and 0.27 for far-red SIF. Nonetheless, the omnidirectional escape factors of individual  
 756 canopy layers were higher, reaching up to 0.65 for red and 0.9 for far-red SIF in the highly  
 757 emissive top 25% of the canopy height (Figure 10b). These numbers and results in Figures 9  
 758 and 10 suggest that oblique multi-directional observations of forest canopies (e.g., with tower-  
 759 based instruments) should capture more SIF photons than a single nadir measurement, and,  
 760 thus, provide a stronger SIF<sub>TOC</sub> signal. Once again, more simulations covering different forest  
 761 types and their natural variability are required to conclude if these interpretations have a general  
 762 applicability or if the white peppermint canopies represent a unique and possibly extreme case..  
 763 Despite a limited size of this study, we demonstrate that the entire 3D structural complexity,  
 764 including woody material, must be taken into account when assessing quantity of SIF photons  
 765 scattered and absorbed by canopy components and those escaping from a forest canopy.

#### 766 ***4.4 Development of DART SIF modelling for large canopies and landscapes***

767 DART SIF simulations for geometrically explicit representations of terrestrial vegetation  
 768 have computational limitations regarding a simulated scene size and a number of objects (i.e.,  
 769 triangular facets) creating 3D mock-ups of plant canopies. Theoretically, one can create an  
 770 extensive landscape occupied with an unlimited population of plants and other 3D objects (e.g.,  
 771 open-water bodies, roads, buildings, etc.), but the SIF simulation, and mainly radiative budget,  
 772 of such a scene might be practically unfeasible as the computer memory and processor  
 773 capabilities are not unlimited. Therefore, another two approaches, allowing more efficient  
 774 simulations of large canopies and extensive landscapes, are being implemented and tested in  
 775 DART: i) SIF modelling for vegetation canopies represented by 3D turbid voxels (i.e., voxels

776 filled with a vegetation turbid medium), and ii) a direct and reverse MC modelling called  
777 DART-Lux (Gastellu-Etchegorry et al. 2020). The latter one is especially highly promising for  
778 simulating extensive SIF<sub>TOC</sub> images. It uses only the landscape elements contributing to the  
779 formation of a simulated image, which decreases the computer time and memory by a factor as  
780 large as 100. Once fully tested and solidified, both approaches will provide DART users with  
781 potential satellite SIF observations adapted to common ground sampling distances of hundreds  
782 of meters. Such simulations could test multiple SIF confounding optical effects, for instance,  
783 those originating from photosynthetically inactive Earth surfaces of rough terrain  
784 configurations resulting in dynamic spatiotemporal irradiation changes and shadow patterns.

### 785 5. Conclusions

786 Physical and technical implementation of discrete anisotropic radiative transfer modelling  
787 for solar-induced chlorophyll fluorescence in geometrically explicit 3D plant canopies was  
788 described and compared with complementary cases simulated in 1D models SCOPE and  
789 mSCOPE. The cross-comparison revealed that DART simulations of SIF<sub>TOC</sub> for geometrically  
790 simple and spatially homogenous canopies produced nearly the same results as both 1D models.  
791 The largest SIF<sub>TOC</sub> differences occurred in very oblique viewing angles that are impacted by  
792 higher modelling uncertainties than the directions closer to nadir.

793 Further exploitation of DART ability to simulate SIF images and radiative budgets of  
794 virtual 3D maize crops showed that the distinction and adjustment of fluorescence efficiencies  
795 for sun- and shade-adapted leaves had a smaller impact on DART simulated SIF<sub>TOC</sub> than an  
796 increase in leaf density (LAI) and local foliage clumping. When analysing nadir SIF<sub>TOC</sub> impacts  
797 by foliar density traits, we found a superior role of LAI over the foliage clumping. Nonetheless,  
798 the foliage clumping was shown to be an important controlling factor of maize and eucalyptus  
799 SIF<sub>TOC</sub> simulated at 686 and 740 nm in oblique viewing directions, and also a crucial driver of  
800 the red SIF balance, i.e., SIF emission and absorption, in vertical profile of irregularly spaced  
801 maize crop with LAI = 2. These study outcomes must be, however, reproduced for other plant  
802 functional types to confirm and investigate further the influences of leaf light intensity  
803 adaptations and density traits on SIF variability inside and at the top of different canopies.

804 DART simulations of two white peppermint eucalyptus stands suggested that woody  
805 material has a significant impact on SIF<sub>TOC</sub>. Trunks and branches cast shadows on  
806 photosynthesizing leaves, decreasing their SIF emissions by about 15% in dense and 8% in

807 sparse canopy simulations. Although the absorbance and reflectance of eucalyptus bark (both  
808 about 50% at 740 nm), in combination with a multiple scattering and absorption by leaves,  
809 nearly doubled the pool of far-red SIF photons in the top 25% part of dense canopy, they  
810 reduced the overall canopy escape of far-red SIF in the nadir viewing direction by 6% and 4%  
811 in the sparse stand. Interestingly, the nadir escape factors of red SIF from dense and sparse  
812 canopies were almost unimpacted by presence of woody material, despite a relatively high 40%  
813 reflectance of bark at 686 nm. These unique results demonstrate that further development of  
814 SIF 3D radiative transfer modelling has a potential to reveal new insights in SIF observations  
815 of spectrally, spatially and topographically heterogeneous vegetated landscapes, acquired at  
816 different spatial scales by proximal, airborne and space-borne optical sensors.

### 817 **Acknowledgments**

818 Authors are grateful to Luke Wallace and Samuel Hillman from the RMIT University in  
819 Melbourne for acquisition and pre-processing of TLS point clouds of the white peppermint  
820 eucalypt trees, permitting their 3D virtual constructions. We also acknowledge constructive  
821 reviews of the anonymous peers that helped us to improve scientific quality and readability of  
822 this manuscript. Contribution of Z. Malenovský was funded by the NASA Earth Science  
823 Division (ESD) in support of the ‘FLuorescence Airborne Research Experiment (FLARE)’ and  
824 by the Australian Research Council Future Fellowship ‘Bridging Scales in Remote Sensing of  
825 Vegetation Stress’ (FT160100477). Contribution of the CESBIO Laboratory authors was  
826 supported by the TOSCA project ‘Fluo3D’ and by the PhD program of the French Space Center  
827 (CNES) and the Centre National de Recherche Scientifique (CNRS). Work of R. Janoutová was  
828 supported by the Ministry of Education, Youth and Sports of CR within the CzeCOS program  
829 (grant LM2018123). Involvement of P. Yang was supported by the Netherlands Organization  
830 for Scientific Research (grant ALWGO.2017.018).

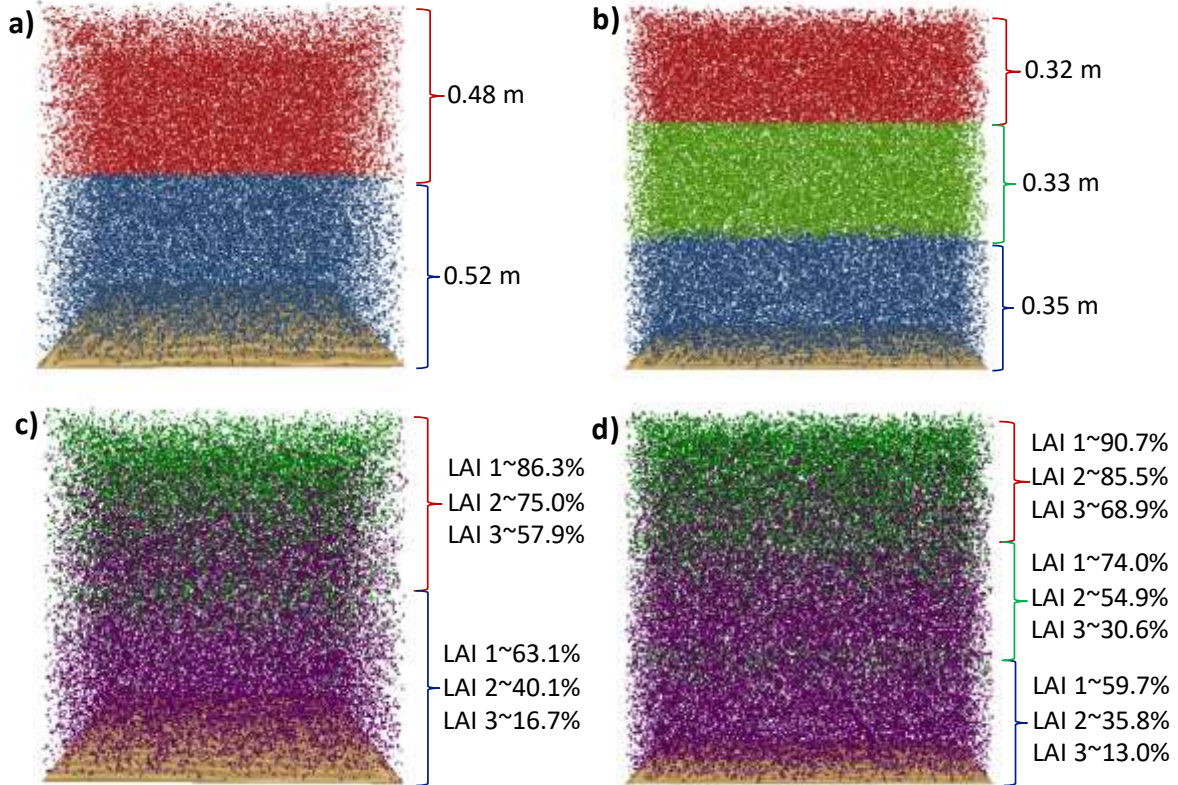
---

831

832 **Appendix A: Comparison of DART and SCOPE/mSCOPE SIF radiative transfers**

833 Since SCOPE and mSCOPE are turbid medium models, we prepared DART 3D scenes  
834 mimicking their 1D canopies as closely as possible. SCOPE, mSCOPE and DART were  
835 adjusted to use the same bottom-of-atmosphere (BOA) solar direct and diffuse irradiance,  
836 simulated with DART atmosphere radiative transfer module using the United States standard  
837 atmosphere gas model (NOAA et al. 1976) and the rural area aerosol model with a visibility of  
838 23 km. The scene was a 1 m height vegetation canopy above a bare soil with three Lambertian  
839 reflectance ( $\rho$ ) properties: i) black soil ( $\rho = 0$ ), ii) half-reflective soil ( $\rho = 0.5$ ), and iii) loamy  
840 gravel brown dark soil with  $\rho$  linearly increasing with wavelength ( $\rho \approx 6\%$  at 550 nm,  $\rho \approx 12\%$   
841 at 686 nm and  $\rho \approx 15\%$  at 740 nm). Every leaf facet had the same specific Lambertian  
842 reflectance and transmittance, i.e., there was no division of leaf optical properties on sunlit or  
843 sun-adapted and shaded or shade-adapted leaves. For the DART-SCOPE comparison, the *eta*  
844 fluorescence weight parameters were forced to one. For the DART-mSCOPE comparison, we  
845 split turbid scenes into two and three almost equally high layers (see Figure A1ab). Leaves of  
846 2- and 3-layer simulations were divided into sunlit and shaded (see % of sunlit leaves in each  
847 layer in Figure A1cd) and the *eta* parameters simulated per layer for both leaf cohorts in  
848 mSCOPE were entered in the corresponding DART simulations. Leaf optical properties were  
849 simulated with the same Fluspect version, using the input parameters listed in Table A1. In  
850 attempt to simulate strong SIF<sub>TOC</sub> signals, the *fqe* values for PSI and PSII were selected close  
851 to their potential maximums. Simulations considered three leaf densities, specified by the leaf  
852 area index (LAI) equal to 1, 2 and 4. In SCOPE simulations, we tested three leaf angle  
853 distributions (LAD): Spherical, Erectophile and Planophile (Danson 1998), whereas we applied  
854 only the Spherical function, the most frequent naturally occurring LAD, in mSCOPE  
855 simulations. All leaves were homogenously distributed throughout the canopies, i.e. the foliage  
856 clumping index (Chen and Black 1992) was equal to 1. The DART leaf facets were equilateral  
857 triangles with the surface area of 0.08 cm<sup>2</sup>. Such small leaf area ensured independency of DART  
858 simulated TOC reflectance and SIF from the solar azimuth angle. The leaf width required for  
859 SCOPE/mSCOPE computations in the hot-spot direction was set to the height of DART facets,  
860 i.e., 0.37 cm. The solar azimuth angle (SAA) was fixed to 311.89° (anticlockwise from South)  
861 and the solar zenith angle (SZA) to 37.94° (i.e., solar elevation angle of 52.06°) as for  
862 Washington D.C. (USA) area (the Beltsville Agricultural Research Center; Lat. 39.03°N, Long.  
863 76.85°W) on 26<sup>th</sup> August 2014 at 14.00 local time (i.e., at 13.50 solar time). Nadir SIF<sub>TOC</sub>

864 radiance [ $\text{W}\cdot\text{m}^{-2}\cdot\mu\text{m}^{-1}\cdot\text{sr}^{-1}$ ] between 640 and 850 nm (1 nm bandwidth) was simulated for all  
 865 combinations of the input parameters with the three RTMs. The obtained PSI, PSII and total  
 866 SIF<sub>TOC</sub> values were compared statistically (as described in Section 2.6).



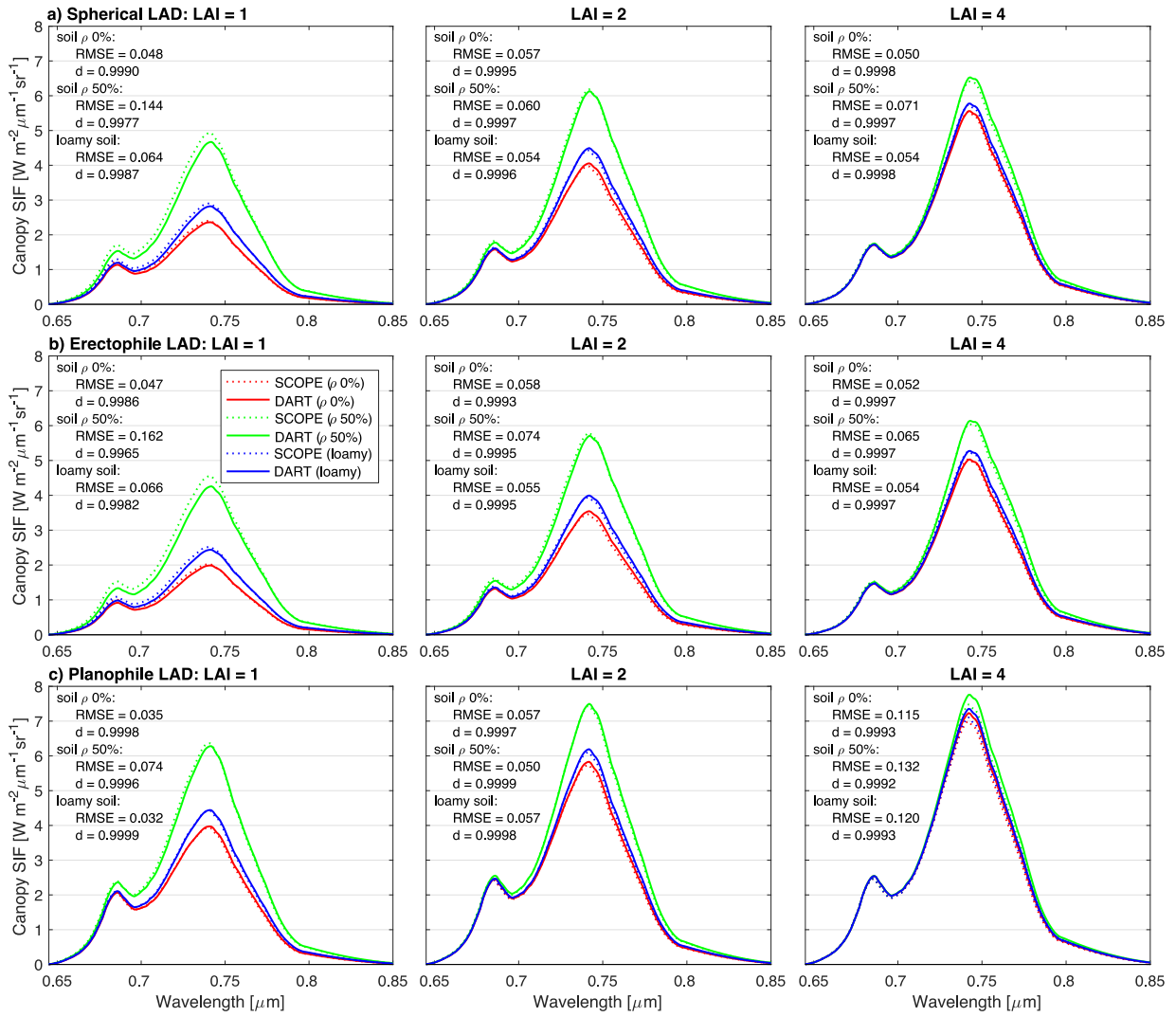
867  
 868 Figure A1. DART representations of a) 2- and b) 3-layered turbid-like canopies designed for comparison  
 869 with the mSCOPE model (numbers indicate the height of each layer). Illustration of sunlit (under direct  
 870 illumination; green) and shaded (under diffuse illumination, violet) triangular leaves for both c) 2- and  
 871 d) 3-layered canopies (numbers indicate % of sunlit leaves per layer for each simulated LAI).  
 872

873 Table A1: Input parameters of the Fluspect model used to simulate optical properties of  
 874 SCOPE/mSCOPE turbid medium leaves and corresponding DART leaves (for explanations of input  
 875 abbreviations see caption of Table 1).

Fluspect inputs	Cab [ $\mu\text{g}\cdot\text{cm}^{-2}$ ]	Car [ $\mu\text{g}\cdot\text{cm}^{-2}$ ]	EWT [cm]	LMA [ $\text{g}\cdot\text{cm}^{-2}$ ]	N	PSI <i>fqe</i>	PSII <i>fqe</i>
(m)SCOPE layers							
mSCOPE first layer (from top)	40	10	0.006	0.0014	1.0	0.006	0.03
SCOPE & mSCOPE second layer	60	15	0.009	0.0021	1.5	0.006	0.03
mSCOPE third layer (from top)	80	20	0.012	0.0028	2	0.006	0.03

876

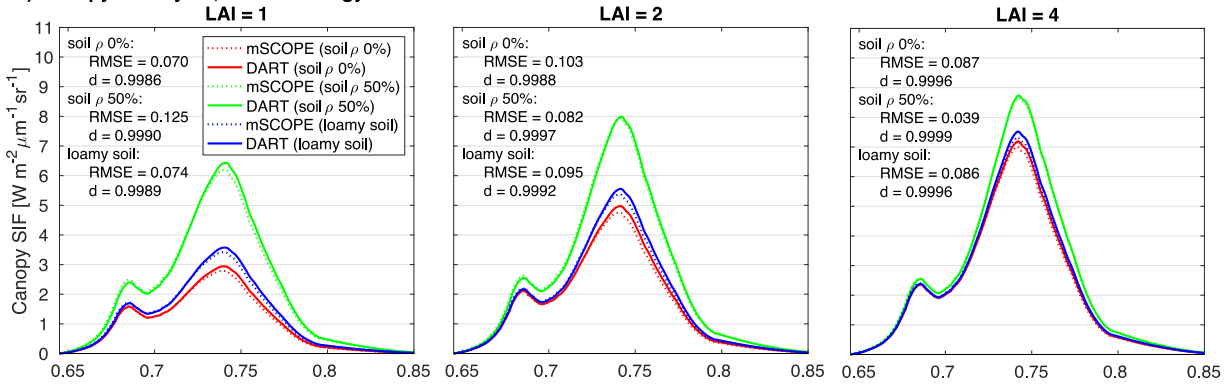
## 2.1 VEGETATION SIMULATED AS FACETS



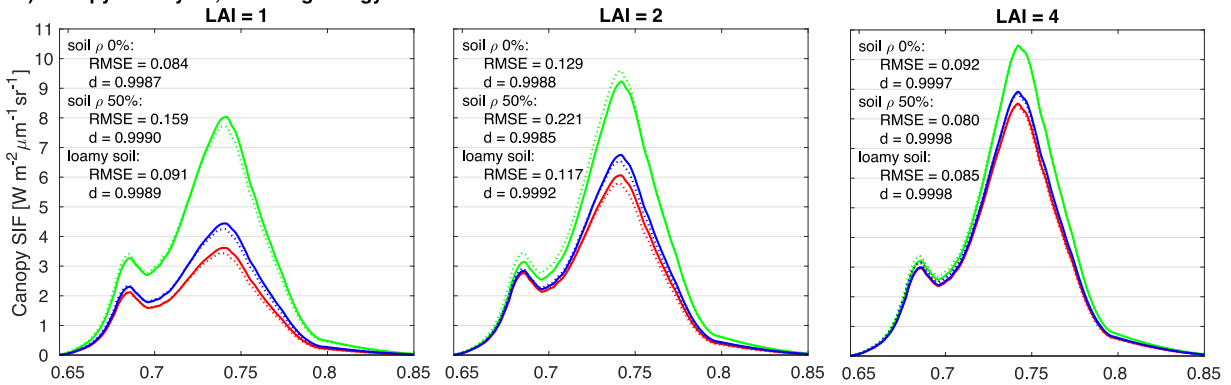
877

878 Figure A2. DART and SCOPE total nadir SIF of vegetation canopies with LAI=1, 2 and 4, three soils ( $\rho$   
 879 = 0%,  $\rho = 50\%$ ,  $\rho =$  loamy dark gravel soil), and with a) Spherical, b) Erectophile, and c) Planophile  
 880 LAD (RMSE ~ root mean square error; d ~ index of agreement: 0 = no agreement, 1 = full agreement).

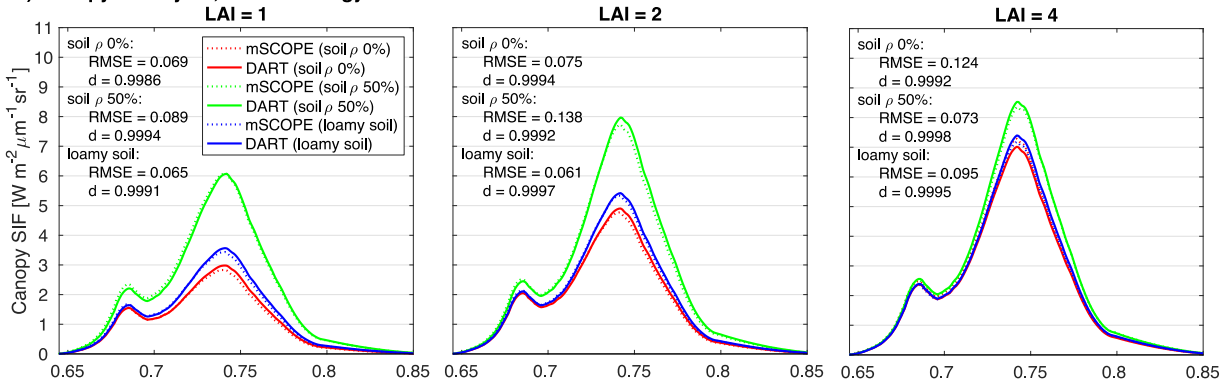
a) Canopy of 2 layers, without energy balance:



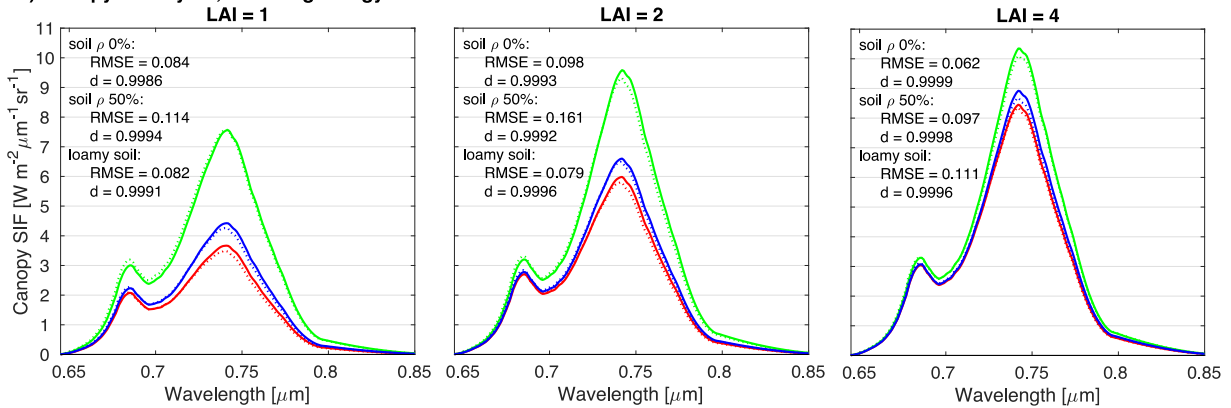
b) Canopy of 2 layers, including energy balance:



c) Canopy of 3 layers, without energy balance:



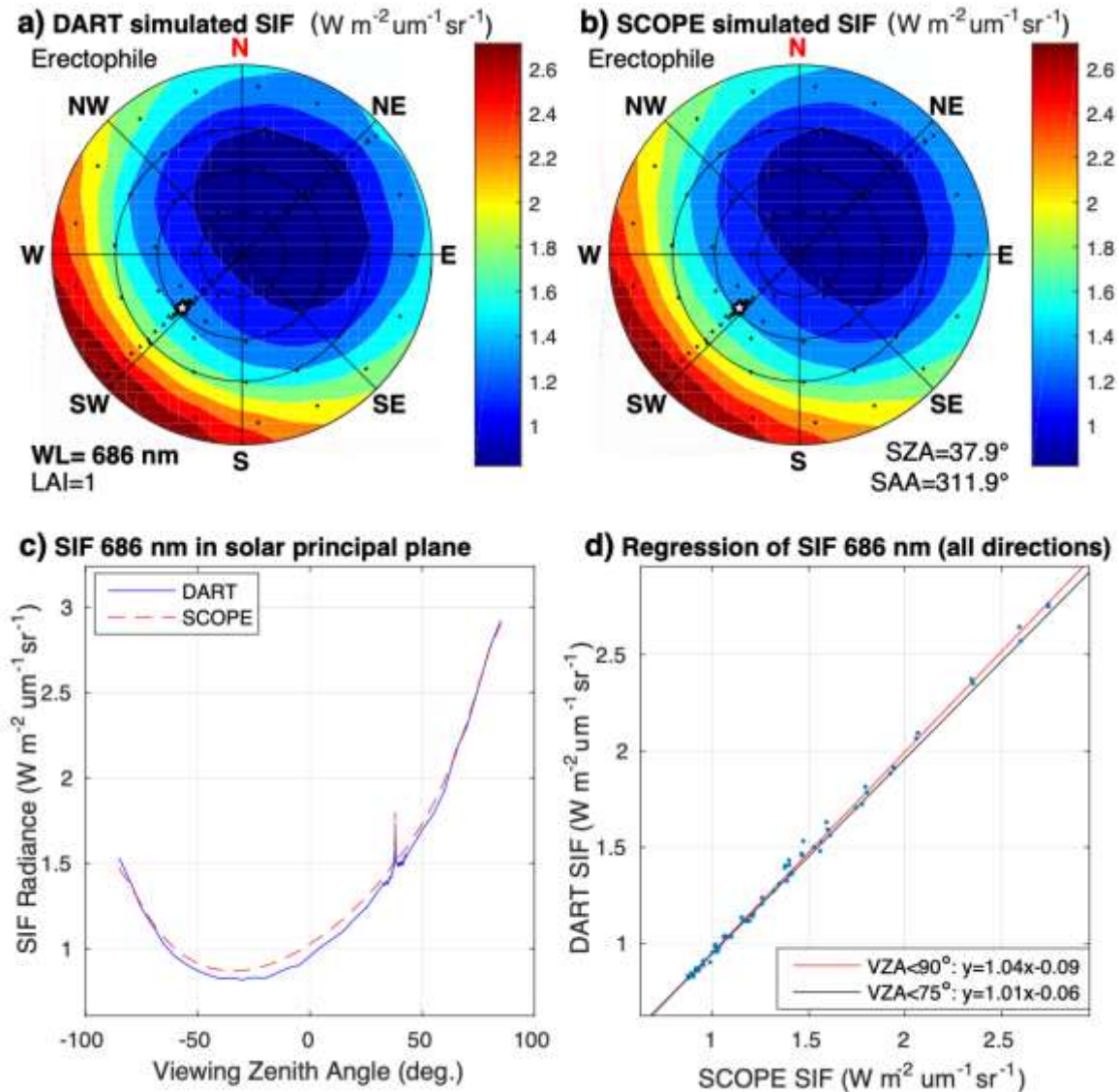
d) Canopy of 3 layers, including energy balance:





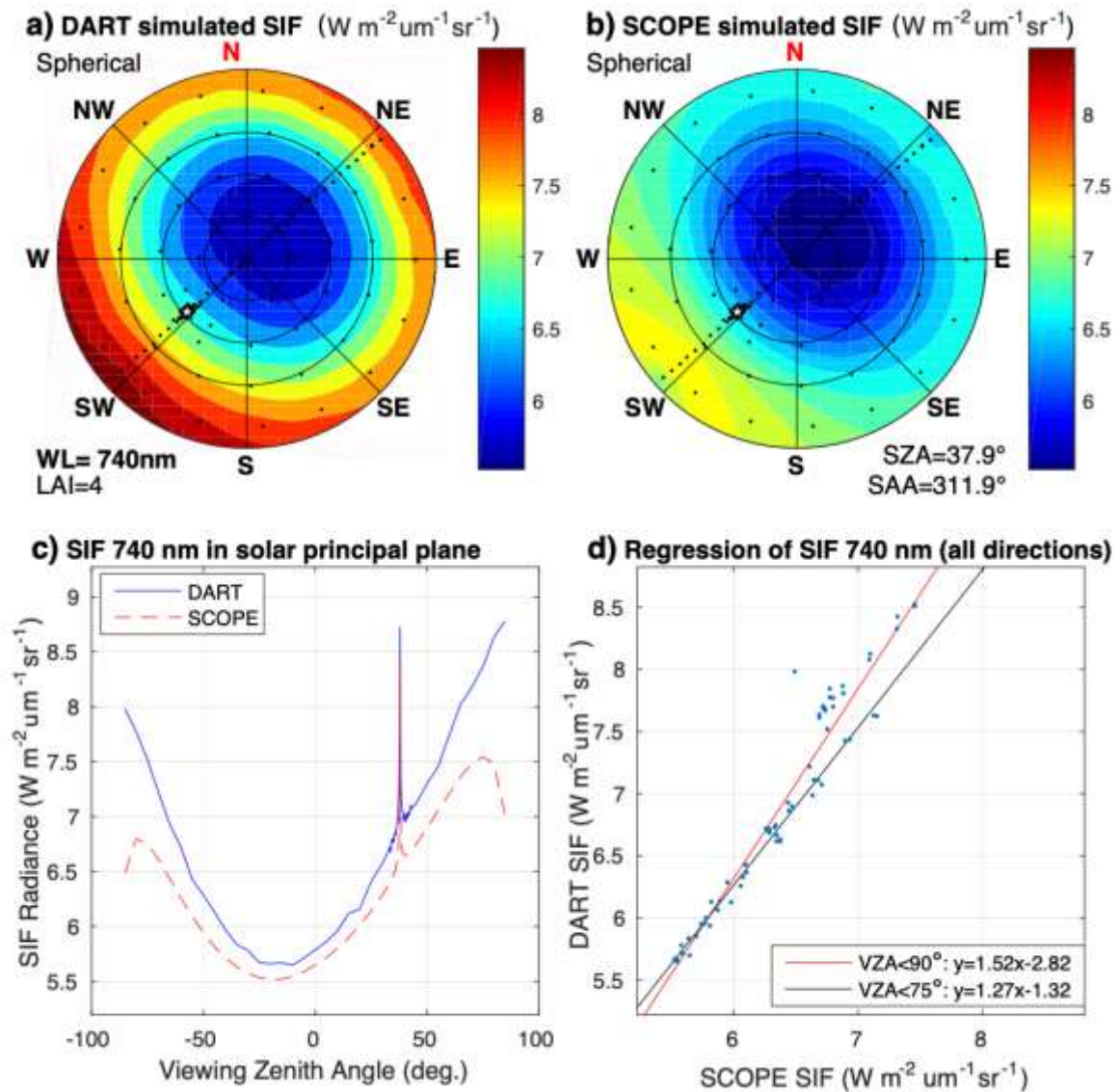
## 2.1 VEGETATION SIMULATED AS FACETS

882 Figure A3. DART and mSCOPE nadir SIF of vegetation canopies simulated with the Spherical LAD,  
 883 three soils ( $\rho = 0\%$ ,  $\rho = 50\%$ ,  $\rho =$  loamy dark gravel soil) in two layers a) without and b) with energy  
 884 balance, and in three layers c) without and d) with energy balance (for abbreviations see Figure A2).



885

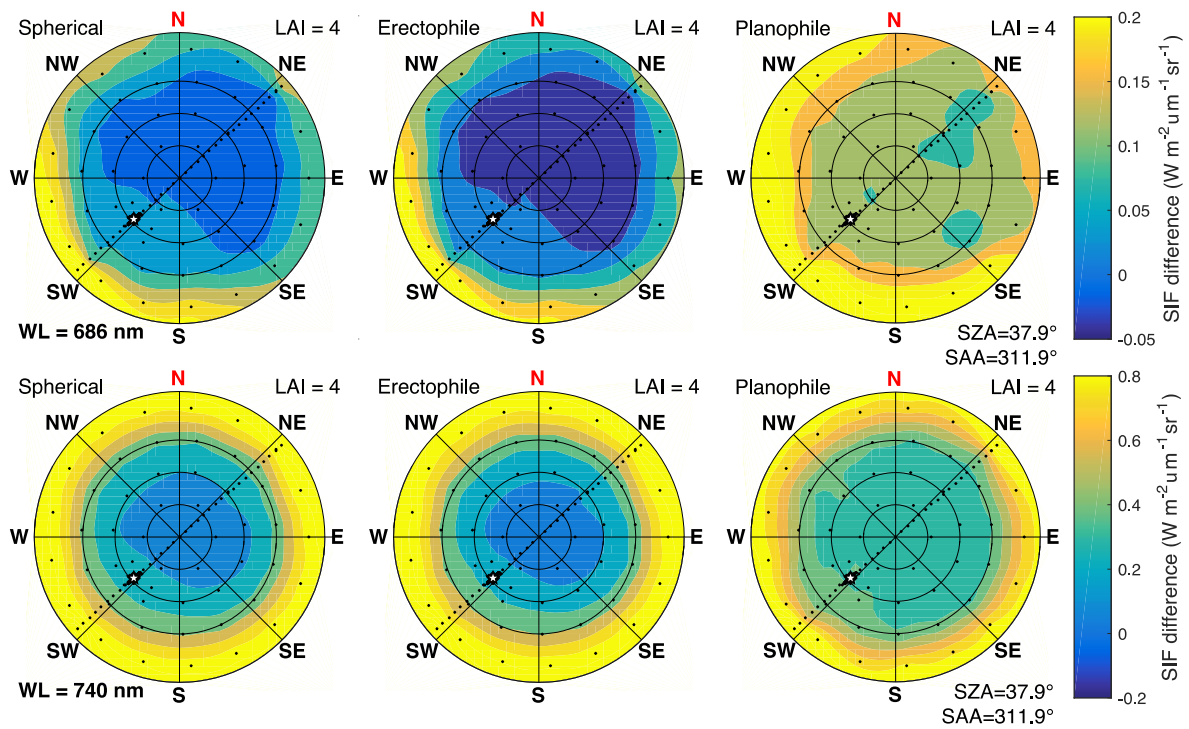
886 Figure A4. Best agreement when comparing a) DART and b) SCOPE multi-angular SIF of a turbid  
 887 medium canopy was found for the Erectophile LAD and a null soil reflectance. SIF radiance in the solar  
 888 principal plane and linear regression of turbid-like DART and turbid SCOPE simulations ( $R^2 = 0.99$ ,  
 889  $RMSE = 0.03$ ,  $d = 1.0$  for all simulated viewing directions, i.e.,  $VZA < 90^\circ$ , and  $RMSE = 0.02$  for  
 890  $VZA < 75^\circ$ ) are shown in c) and d) graphs, respectively (for abbreviations and symbols see Figure 5).



891

892 Figure A5. Worst agreement when comparing a) DART and b) SCOPE multi-angular SIF of turbid  
 893 medium canopy with the Spherical LAD and a 50% reflective soil. SIF radiance in the solar principal  
 894 plane and linear regression of turbid-like DART and turbid SCOPE simulations ( $R^2 = 0.94$ , RMSE =  
 895 0.21,  $d = 1.0$  for  $VZA < 90^\circ$  and  $R^2 = 0.99$ , RMSE = 0.07 for  $VZA < 75^\circ$ ) are shown in c) and d) graphs,  
 896 respectively (for abbreviations and symbols see Figure 5).

## 2.1 VEGETATION SIMULATED AS FACETS



897

898 Figure A6. DART-SCOPE differences in multi-angular SIF radiance at 686 and 740 nm for a canopy  
 899 with LAI = 4, having Spherical, Erectophile and Planophile LADs (the white star shows the solar  
 900 position and black dots indicate the simulated viewing directions; for abbreviations see Figure 5).

901

### 902 References

- 903 Aasen, H., Van Wittenberghe, S., Sabater Medina, N., Damm, A., Goulas, Y., Wieneke, S.,  
 904 Hueni, A., Malenovský, Z., Alonso, L., Pacheco-Labrador, J., Cendrero-Mateo, P.M.,  
 905 Tomelleri, E., Burkart, A., Cogliati, S., Rascher, U., & Mac Arthur, A. (2019). Sun-Induced  
 906 Chlorophyll Fluorescence II: Review of Passive Measurement Setups, Protocols, and Their  
 907 Application at the Leaf to Canopy Level. *Remote Sensing*, *11*, 927
- 908 Ashley, M.D., & Rea, J. (1975). Seasonal vegetation differences from ERTS imagery. *Journal*  
 909 *of American Society of Photogrammetry*, *41*, 713-719
- 910 Bendig, J., Malenovský, Z., Gautam, D., & Lucieer, A. (2020). Solar-Induced Chlorophyll  
 911 Fluorescence Measured From an Unmanned Aircraft System: Sensor Etaloning and  
 912 Platform Motion Correction. *IEEE Transactions on Geoscience and Remote Sensing*, *58*,  
 913 3437-3444

- 914 Blair, B.O., & Baumgardner, M.F. (1977). Detection of the Green and Brown Wave in  
 915 Hardwood Canopy Covers Using Multidate, Multispectral Data from LANDSAT-11.  
 916 *Agronomy Journal*, 69, 808-811
- 917 Blender (2007). <https://www.blender.org/> (12 February 2020)
- 918 Chen, J.M., & Black, T.A. (1992). Defining leaf area index for non-flat leaves. *Plant, Cell &*  
 919 *Environment*, 15, 421-429
- 920 Croft, H., Chen, J.M., Wang, R., Mo, G., Luo, S., Luo, X., He, L., Gonsamo, A., Arabian, J.,  
 921 Zhang, Y., Simic-Milas, A., Noland, T.L., He, Y., Homolová, L., Malenovský, Z., Yi, Q.,  
 922 Beringer, J., Amiri, R., Hutley, L., Arellano, P., Stahl, C., & Bonal, D. (2020). The global  
 923 distribution of leaf chlorophyll content. *Remote Sensing of Environment*, 236, 111479
- 924 Danson, F.M. (1998). Teaching the physical principles of vegetation canopy reflectance using  
 925 the SAIL model. *Photogrammetric Engineering & Remote Sensing*, 64, 809-812
- 926 DART (2019).  
 927 [https://dart.omp.eu/Public/documentation/contenu/documentation/DART\\_handbook.pdf](https://dart.omp.eu/Public/documentation/contenu/documentation/DART_handbook.pdf)  
 928 (6 February 2020)
- 929 DART (2020).  
 930 [https://dart.omp.eu/Public/documentation/contenu/documentation/DART\\_User\\_Manual.p](https://dart.omp.eu/Public/documentation/contenu/documentation/DART_User_Manual.pdf)  
 931 [df](https://dart.omp.eu/Public/documentation/contenu/documentation/DART_User_Manual.pdf) (6 February 2020)
- 932 Féret, J.B., Berger, K., de Boissieu, F., & Malenovský, Z. (2020). PROSPECT-PRO for  
 933 estimating content of nitrogen-containing leaf proteins and other carbon-based  
 934 constituents. *Remote Sensing of Environment*, in review
- 935 Féret, J.B., Gitelson, A.A., Noble, S.D., & Jacquemoud, S. (2017). PROSPECT-D: Towards  
 936 modeling leaf optical properties through a complete lifecycle. *Remote Sensing of*  
 937 *Environment*, 193, 204-215
- 938 Frankenberg, C., Butz, A., & Toon, G.C. (2011). Disentangling chlorophyll fluorescence from  
 939 atmospheric scattering effects in O2 A-band spectra of reflected sun-light. *Geophysical*  
 940 *Research Letters*, 38
- 941 Gamon, J.A., Somers, B., Malenovský, Z., Middleton, E.M., Rascher, U., & Schaepman, M.E.  
 942 (2019). Assessing Vegetation Function with Imaging Spectroscopy. *Surveys in*  
 943 *Geophysics*, 40, 489-513
- 944 Gastellu-Etchegorry, J.-P., Wang, Y., Regaieg, O., Yin, T., Malenovský, Z., Zhen, Z., Yang,  
 945 X., Tao, Z., Landier, L., Al Bitar, A., Deschamps, A., Lauret, N., Guilleux, J., Chavanon,

## 2.1 VEGETATION SIMULATED AS FACETS

- 946 E., Cao, B., Qi, J., Kallel, A., Mitraka, Z., Chrysoulakis, N., Cook, B., & Morton, D. (2020).  
947 Recent improvements in the DART model for atmosphere, topography, large landscape,  
948 chlorophyll fluorescence, satellite image inversion. In, *IEEE International Geoscience and*  
949 *Remote Sensing Symposium* (p. 5). Virtual Symposium: IEEE
- 950 Gastellu-Etchegorry, J.-P., Yin, T., Lauret, N., Cajgfinger, T., Gregoire, T., Grau, E., Feret, J.-  
951 B., Lopes, M., Guilleux, J., Dedieu, G., Malenovský, Z., Cook, B., Morton, D., Rubio, J.,  
952 Durrieu, S., Cazanave, G., Martin, E., & Ristorcelli, T. (2015). Discrete Anisotropic  
953 Radiative Transfer (DART 5) for Modeling Airborne and Satellite Spectroradiometer and  
954 LIDAR Acquisitions of Natural and Urban Landscapes. *Remote Sensing*, 7, 1667-1701
- 955 Gastellu-Etchegorry, J.P. (2008). 3D modeling of satellite spectral images, radiation budget and  
956 energy budget of urban landscapes. *Meteorology and Atmospheric Physics*, 102, 187
- 957 Gastellu-Etchegorry, J.P., Demarez, V., Pinel, V., & Zagolski, F. (1996). Modeling radiative  
958 transfer in heterogeneous 3-D vegetation canopies. *Remote Sensing of Environment*, 58,  
959 131-156
- 960 Gastellu-Etchegorry, J.P., Lauret, N., Yin, T., Landier, L., Kallel, A., Malenovský, Z., Bitar,  
961 A.A., Aval, J., Benhmida, S., Qi, J., Medjdoub, G., Guilleux, J., Chavanon, E., Cook, B.,  
962 Morton, D., Chrysoulakis, N., & Mitraka, Z. (2017). DART: Recent Advances in Remote  
963 Sensing Data Modeling With Atmosphere, Polarization, and Chlorophyll Fluorescence.  
964 *IEEE Journal of Selected Topics in Applied Earth Observations and Remote Sensing*, 10,  
965 2640-2649
- 966 Gastellu-Etchegorry, J.P., Martin, E., & Gascon, F. (2004). DART: a 3D model for simulating  
967 satellite images and studying surface radiation budget. *International Journal of Remote*  
968 *Sensing*, 25, 73-96
- 969 Givnish, T.J. (1988). Adaptation to Sun and Shade: a Whole-Plant Perspective. *Functional*  
970 *Plant Biology*, 15, 63-92
- 971 Guan, K., Pan, M., Li, H., Wolf, A., Wu, J., Medvigy, D., Caylor, K.K., Sheffield, J., Wood,  
972 E.F., Malhi, Y., Liang, M., Kimball, J.S., Saleska, Scott R., Berry, J., Joiner, J., &  
973 Lyapustin, A.I. (2015). Photosynthetic seasonality of global tropical forests constrained by  
974 hydroclimate. *Nature Geoscience*, 8, 284-289
- 975 Guanter, L., Alonso, L., Gómez-Chova, L., Amorós-López, J., Vila, J., & Moreno, J. (2007).  
976 Estimation of solar-induced vegetation fluorescence from space measurements.  
977 *Geophysical Research Letters*, 34

- 978 Guanter, L., Zhang, Y., Jung, M., Joiner, J., Voigt, M., Berry, J.A., Frankenberg, C., Huete,  
 979 A.R., Zarco-Tejada, P., Lee, J.-E., Moran, M.S., Ponce-Campos, G., Beer, C., Camps-  
 980 Valls, G., Buchmann, N., Gianelle, D., Klumpp, K., Cescatti, A., Baker, J.M., & Griffis,  
 981 T.J. (2014). Global and time-resolved monitoring of crop photosynthesis with chlorophyll  
 982 fluorescence. *Proceedings of the National Academy of Sciences*, *111*, E1327-E1333
- 983 He, L., Chen, J.M., Liu, J., Mo, G., & Joiner, J. (2017). Angular normalization of GOME-2  
 984 Sun-induced chlorophyll fluorescence observation as a better proxy of vegetation  
 985 productivity. *Geophysical Research Letters*, *44*, 5691-5699
- 986 He, L., Magney, T., Dutta, D., Yin, Y., Köhler, P., Grossmann, K., Stutz, J., Dold, C., Hatfield,  
 987 J., Guan, K., Peng, B., & Frankenberg, C. (2020). From the Ground to Space: Using Solar-  
 988 Induced Chlorophyll Fluorescence to Estimate Crop Productivity. *Geophysical Research*  
 989 *Letters*, *47*, e2020GL087474
- 990 Hernández-Clemente, R., North, P.R.J., Hornero, A., & Zarco-Tejada, P.J. (2017). Assessing  
 991 the effects of forest health on sun-induced chlorophyll fluorescence using the  
 992 FluorFLIGHT 3-D radiative transfer model to account for forest structure. *Remote Sensing*  
 993 *of Environment*, *193*, 165-179
- 994 Hosgood, B., Jacquemoud, S., Andreoli, G., Verdebout, J., Pedrini, A., & Schmuck, G. (1994).  
 995 Leaf Optical Properties Experiment 93 (LOPEX93). In, *European Commission No. EUR*  
 996 *16095 EN*. Joint Research Centre, Institute for Remote Sensing Applications
- 997 Jacquemoud, S., & Baret, F. (1990). PROSPECT: A model of leaf optical properties spectra.  
 998 *Remote Sensing of Environment*, *34*, 75-91
- 999 Janoutová, R., Homolová, L., Malenovský, Z., Hanuš, J., Lauret, N., & Gastellu-Etchegorry,  
 1000 J.-P. (2019). Influence of 3D Spruce Tree Representation on Accuracy of Airborne and  
 1001 Satellite Forest Reflectance Simulated in DART. *Forests*, *10*, 292
- 1002 Joiner, J., Yoshida, Y., Vasilkov, A.P., Yoshida, Y., Corp, L.A., & Middleton, E.M. (2011).  
 1003 First observations of global and seasonal terrestrial chlorophyll fluorescence from space.  
 1004 *Biogeosciences*, *8*, 637-651
- 1005 Kallel, A. (2020). FluLCVRT: Reflectance and fluorescence of leaf and canopy modeling based  
 1006 on Monte Carlo vector radiative transfer simulation. *Journal of Quantitative Spectroscopy*  
 1007 *and Radiative Transfer*, *253*, 107183
- 1008 Kallel, A., & Nilson, T. (2013). Revisiting the vegetation hot spot modeling: Case of  
 1009 Poisson/Binomial leaf distributions. *Remote Sensing of Environment*, *130*, 188-204



## 2.1 VEGETATION SIMULATED AS FACETS

- 1010 Köhler, P., Guanter, L., Kobayashi, H., Walther, S., & Yang, W. (2018). Assessing the potential  
1011 of sun-induced fluorescence and the canopy scattering coefficient to track large-scale  
1012 vegetation dynamics in Amazon forests. *Remote Sensing of Environment*, 204, 769-785
- 1013 Leuning, R., Kelliher, F.M., De Pury, D.G.G., & Schulze, E.D. (1995). Leaf nitrogen,  
1014 photosynthesis, conductance and transpiration: scaling from leaves to canopies. *Plant, Cell  
1015 & Environment*, 18, 1183-1200
- 1016 Liu, W., Atherton, J., Möttus, M., Gastellu-Etchegorry, J.-P., Malenovský, Z., Raunonen, P.,  
1017 Åkerblom, M., Mäkipää, R., & Porcar-Castell, A. (2019a). Simulating solar-induced  
1018 chlorophyll fluorescence in a boreal forest stand reconstructed from terrestrial laser  
1019 scanning measurements. *Remote Sensing of Environment*, 232, 111274
- 1020 Liu, X., Guanter, L., Liu, L., Damm, A., Malenovský, Z., Rascher, U., Peng, D., Du, S., &  
1021 Gastellu-Etchegorry, J.-P. (2019b). Downscaling of solar-induced chlorophyll  
1022 fluorescence from canopy level to photosystem level using a random forest model. *Remote  
1023 Sensing of Environment*, 231, 110772
- 1024 Malenovský, Z., Homolová, L., Lukeš, P., Buddenbaum, H., Verrelst, J., Alonso, L.,  
1025 Schaepman, M.E., Lauret, N., & Gastellu-Etchegorry, J.-P. (2019). Variability and  
1026 Uncertainty Challenges in Scaling Imaging Spectroscopy Retrievals and Validations from  
1027 Leaves Up to Vegetation Canopies. *Surveys in Geophysics*, 40, 631-656
- 1028 Malenovský, Z., Homolová, L., Zurita-Milla, R., Lukeš, P., Kaplan, V., Hanuš, J., Gastellu-  
1029 Etchegorry, J.-P., & Schaepman, M.E. (2013). Retrieval of spruce leaf chlorophyll content  
1030 from airborne image data using continuum removal and radiative transfer. *Remote Sensing  
1031 of Environment*, 131, 85-102
- 1032 Malenovský, Z., Martin, E., Homolová, L., Gastellu-Etchegorry, J.-P., Zurita-Milla, R.,  
1033 Schaepman, M.E., Pokorný, R., Clevers, J.G.P.W., & Cudlín, P. (2008). Influence of  
1034 woody elements of a Norway spruce canopy on nadir reflectance simulated by the DART  
1035 model at very high spatial resolution. *Remote Sensing of Environment*, 112, 1-18
- 1036 Malenovský, Z., Ufer, C., Lhotáková, Z., Clevers, J.G.P.W., Schaepman, M.E., Albrechtová,  
1037 J., & Cudlín, P. (2006). A new hyperspectral index for chlorophyll estimation of a forest  
1038 canopy: Area under curve normalised to maximal band depth between 650-725 nm *EARSel  
1039 eProceedings*, 5, 161-172
- 1040 Migliavacca, M., Perez-Priego, O., Rossini, M., El-Madany, T.S., Moreno, G., van der Tol, C.,  
1041 Rascher, U., Berninger, A., Bessenbacher, V., Burkart, A., Carrara, A., Fava, F., Guan,



- 1042 J.H., Hammer, T.W., Henkel, K., Juarez-Alcalde, E., Julitta, T., Kolle, O., Martín, M.P.,  
 1043 Musavi, T., Pacheco-Labrador, J., Pérez-Burgueño, A., Wutzler, T., Zaehle, S., &  
 1044 Reichstein, M. (2017). Plant functional traits and canopy structure control the relationship  
 1045 between photosynthetic CO<sub>2</sub> uptake and far-red sun-induced fluorescence in a  
 1046 Mediterranean grassland under different nutrient availability. *New Phytologist*, 214, 1078-  
 1047 1091
- 1048 Mohammed, G.H., Colombo, R., Middleton, E.M., Rascher, U., van der Tol, C., Nedbal, L.,  
 1049 Goulas, Y., Pérez-Priego, O., Damm, A., Meroni, M., Joiner, J., Cogliati, S., Verhoef, W.,  
 1050 Malenovský, Z., Gastellu-Etchegorry, J.-P., Miller, J.R., Guanter, L., Moreno, J., Moya, I.,  
 1051 Berry, J.A., Frankenberg, C., & Zarco-Tejada, P.J. (2019). Remote sensing of solar-  
 1052 induced chlorophyll fluorescence (SIF) in vegetation: 50 years of progress. *Remote Sensing*  
 1053 *of Environment*, 231, 111177
- 1054 Myneni, R.B., & Ross, J. (2012). *Photon-Vegetation Interactions: Applications in Optical*  
 1055 *Remote Sensing and Plant Ecology*. Springer Berlin Heidelberg
- 1056 Niinemets, Ü., Keenan, T.F., & Hallik, L. (2015). A worldwide analysis of within-canopy  
 1057 variations in leaf structural, chemical and physiological traits across plant functional types.  
 1058 *New Phytologist*, 205, 973-993
- 1059 NOAA, NASA, & Air-Force, U.S. (1976). *U.S. Standard Atmosphere, 1976*. Washington D.C.:  
 1060 NOAA, U.S. Government Printing Office
- 1061 Nobel, P.S. (1976). Photosynthetic Rates of Sun versus Shade Leaves of *Hyptis emoryi* Torr.  
 1062 *Plant Physiology*, 58, 218-223
- 1063 North, P.R.J. (1996). Three-dimensional forest light interaction model using a monte carlo  
 1064 method. *IEEE Transactions on Geoscience and Remote Sensing*, 34, 946-956
- 1065 Pacheco-Labrador, J., Perez-Priego, O., El-Madany, T.S., Julitta, T., Rossini, M., Guan, J.,  
 1066 Moreno, G., Carvalhais, N., Martín, M.P., Gonzalez-Cascon, R., Kolle, O., Reischtein, M.,  
 1067 van der Tol, C., Carrara, A., Martini, D., Hammer, T.W., Moossen, H., & Migliavacca, M.  
 1068 (2019). Multiple-constraint inversion of SCOPE. Evaluating the potential of GPP and SIF  
 1069 for the retrieval of plant functional traits. *Remote Sensing of Environment*, 234, 111362
- 1070 Pedrós, R., Goulas, Y., Jacquemoud, S., Louis, J., & Moya, I. (2010). FluorMODleaf: A new  
 1071 leaf fluorescence emission model based on the PROSPECT model. *Remote Sensing of*  
 1072 *Environment*, 114, 155-167

## 2.1 VEGETATION SIMULATED AS FACETS

- 1073 Peng, B., Guan, K., Zhou, W., Jiang, C., Frankenberg, C., Sun, Y., He, L., & Köhler, P. (2020).  
1074 Assessing the benefit of satellite-based Solar-Induced Chlorophyll Fluorescence in crop  
1075 yield prediction. *International Journal of Applied Earth Observation and Geoinformation*,  
1076 90, 102126
- 1077 Pradal, C., Dufour-Kowalski, S., Boudon, F., Fournier, C., & Godin, C. (2008). OpenAlea: a  
1078 visual programming and component-based software platform for plant modelling.  
1079 *Functional Plant Biology*, 35, 751-760
- 1080 Rosema, A., Verhoef, W., Schroote, J., & Snel, J.F.H. (1991). Simulating fluorescence light-  
1081 canopy interaction in support of laser-induced fluorescence measurements. *Remote Sensing*  
1082 *of Environment*, 37, 117-130
- 1083 Sakai, Y., Kobayashi, H., & Kato, T. (2020). FLiES-SIF ver. 1.0: Three-dimensional radiative  
1084 transfer model for estimating solar induced fluorescence. *Geosci. Model Dev. Discuss.*,  
1085 2020, 1-36
- 1086 Sloup, P. (2013). [https://is.muni.cz/th/325196/fi\\_m/?lang=en](https://is.muni.cz/th/325196/fi_m/?lang=en) (18 February 2020)
- 1087 Sušila, P., & Nauš, J. (2007). A Monte Carlo study of the chlorophyll fluorescence emission  
1088 and its effect on the leaf spectral reflectance and transmittance under various conditions.  
1089 *Photochemical & Photobiological Sciences*, 6, 894-902
- 1090 Tong, C., Bao, Y., Zhao, F., Fan, C., Li, Z., & Huang, Q. (2021). Evaluation of the FluorWPS  
1091 Model and Study of the Parameter Sensitivity for Simulating Solar-Induced Chlorophyll  
1092 Fluorescence. *Remote Sensing*, 13
- 1093 van der Tol, C., Rossini, M., Cogliati, S., Verhoef, W., Colombo, R., Rascher, U., &  
1094 Mohammed, G. (2016). A model and measurement comparison of diurnal cycles of sun-  
1095 induced chlorophyll fluorescence of crops. *Remote Sensing of Environment*, 186, 663-677
- 1096 van der Tol, C., Verhoef, W., Timmermans, J., Verhoef, A., & Su, Z. (2009). An integrated  
1097 model of soil-canopy spectral radiances, photosynthesis, fluorescence, temperature and  
1098 energy balance. *Biogeosciences*, 6, 3109-3129
- 1099 van der Tol, C., Vilfan, N., Dauwe, D., Cendrero-Mateo, M.P., & Yang, P. (2019). The  
1100 scattering and re-absorption of red and near-infrared chlorophyll fluorescence in the  
1101 models Fluspect and SCOPE. *Remote Sensing of Environment*, 232, 111292
- 1102 Verhoef, W. (1984). Light scattering by leaf layers with application to canopy reflectance  
1103 modeling: The SAIL model. *Remote Sensing of Environment*, 16, 125-141

- 1104 Verrelst, J., Malenovský, Z., Van der Tol, C., Camps-Valls, G., Gastellu-Etchegorry, J.-P.,  
 1105 Lewis, P., North, P., & Moreno, J. (2019). Quantifying Vegetation Biophysical Variables  
 1106 from Imaging Spectroscopy Data: A Review on Retrieval Methods. *Surveys in Geophysics*,  
 1107 40, 589-629
- 1108 Verrelst, J., & Rivera, J.P. (2017). Chapter 16 - A Global Sensitivity Analysis Toolbox to  
 1109 Quantify Drivers of Vegetation Radiative Transfer Models. In G.P. Petropoulos, & P.K.  
 1110 Srivastava (Eds.), *Sensitivity Analysis in Earth Observation Modelling* (pp. 319-339):  
 1111 Elsevier
- 1112 Verrelst, J., Schaepman, M.E., Malenovský, Z., & Clevers, J.G.P.W. (2010). Effects of woody  
 1113 elements on simulated canopy reflectance: Implications for forest chlorophyll content  
 1114 retrieval. *Remote Sensing of Environment*, 114, 647-656
- 1115 Verroust, A., & Lazarus, F. (1999). Extracting skeletal curves from 3D scattered data. In,  
 1116 *Proceedings Shape Modeling International '99. International Conference on Shape*  
 1117 *Modeling and Applications* (pp. 194-201)
- 1118 Vilfan, N., van der Tol, C., Muller, O., Rascher, U., & Verhoef, W. (2016). Fluspect-B: A model  
 1119 for leaf fluorescence, reflectance and transmittance spectra. *Remote Sensing of*  
 1120 *Environment*, 186, 596-615
- 1121 Vilfan, N., van der Tol, C., & Verhoef, W. (2019). Estimating photosynthetic capacity from  
 1122 leaf reflectance and Chl fluorescence by coupling radiative transfer to a model for  
 1123 photosynthesis. *New Phytologist*, 223, 487-500
- 1124 Vilfan, N., Van der Tol, C., Yang, P., Wyber, R., Malenovský, Z., Robinson, S.A., & Verhoef,  
 1125 W. (2018). Extending Fluspect to simulate xanthophyll driven leaf reflectance dynamics.  
 1126 *Remote Sensing of Environment*, 211, 345-356
- 1127 Wang, C., Guan, K., Peng, B., Chen, M., Jiang, C., Zeng, Y., Wu, G., Wang, S., Wu, J., Yang,  
 1128 X., Frankenberg, C., Köhler, P., Berry, J., Bernacchi, C., Zhu, K., Alden, C., & Miao, G.  
 1129 (2020). Satellite footprint data from OCO-2 and TROPOMI reveal significant spatio-  
 1130 temporal and inter-vegetation type variabilities of solar-induced fluorescence yield in the  
 1131 U.S. Midwest. *Remote Sensing of Environment*, 241, 111728
- 1132 Widlowski, J.-L., Mio, C., Disney, M., Adams, J., Andredakis, I., Atzberger, C., Brennan, J.,  
 1133 Busetto, L., Chelle, M., Ceccherini, G., Colombo, R., Côté, J.-F., Eemäe, A., Essery, R.,  
 1134 Gastellu-Etchegorry, J.-P., Gobron, N., Grau, E., Haverd, V., Homolová, L., Huang, H.,  
 1135 Hunt, L., Kobayashi, H., Koetz, B., Kuusk, A., Kuusk, J., Lang, M., Lewis, P.E., Lovell,

## 2.1 VEGETATION SIMULATED AS FACETS

- 1136 J.L., Malenovsky, Z., Meroni, M., Morsdorf, F., Möttus, M., Ni-Meister, W., Pinty, B.,  
1137 Rautiainen, M., Schlerf, M., Somers, B., Stuckens, J., Verstraete, M.M., Yang, W., Zhao,  
1138 F., & Zenone, T. (2015). The fourth phase of the radiative transfer model intercomparison  
1139 (RAMI) exercise: Actual canopy scenarios and conformity testing. *Remote Sensing of*  
1140 *Environment*, 169, 418-437
- 1141 Willmott, C.J. (1981). On the validation of models. *Physical Geography*, 2, 184-194
- 1142 Wyber, R., Malenovsky, Z., Ashcroft, M., Osmond, B., & Robinson, S. (2017). Do Daily and  
1143 Seasonal Trends in Leaf Solar Induced Fluorescence Reflect Changes in Photosynthesis,  
1144 Growth or Light Exposure? *Remote Sensing*, 9, 604
- 1145 Yang, P., Prikaziuk, E., Verhoef, W., & van der Tol, C. (2020a). SCOPE 2.0: A model to  
1146 simulate vegetated land surface fluxes and satellite signals. *Geosci. Model Dev. Discuss.*,  
1147 2020, 1-26
- 1148 Yang, P., & van der Tol, C. (2018). Linking canopy scattering of far-red sun-induced  
1149 chlorophyll fluorescence with reflectance. *Remote Sensing of Environment*, 209, 456-467
- 1150 Yang, P., van der Tol, C., Campbell, P.K.E., & Middleton, E.M. (2020b). Fluorescence  
1151 Correction Vegetation Index (FCVI): A physically based reflectance index to separate  
1152 physiological and non-physiological information in far-red sun-induced chlorophyll  
1153 fluorescence. *Remote Sensing of Environment*, 240, 111676
- 1154 Yang, P., Verhoef, W., & van der Tol, C. (2017). The mSCOPE model: A simple adaptation to  
1155 the SCOPE model to describe reflectance, fluorescence and photosynthesis of vertically  
1156 heterogeneous canopies. *Remote Sensing of Environment*, 201, 1-11
- 1157 Yin, T., Gastellu-Etchegorry, J.-P., Lauret, N., Grau, E., & Rubio, J. (2013). A new approach  
1158 of direction discretization and oversampling for 3D anisotropic radiative transfer modeling.  
1159 *Remote Sensing of Environment*, 135, 213-223
- 1160 Zeng, Y., Badgley, G., Dechant, B., Ryu, Y., Chen, M., & Berry, J.A. (2019). A practical  
1161 approach for estimating the escape ratio of near-infrared solar-induced chlorophyll  
1162 fluorescence. *Remote Sensing of Environment*, 232, 111209
- 1163 Zhang, Z., Zhang, Y., Porcar-Castell, A., Joiner, J., Guanter, L., Yang, X., Migliavacca, M., Ju,  
1164 W., Sun, Z., Chen, S., Martini, D., Zhang, Q., Li, Z., Cleverly, J., Wang, H., & Goulas, Y.  
1165 (2020). Reduction of structural impacts and distinction of photosynthetic pathways in a  
1166 global estimation of GPP from space-borne solar-induced chlorophyll fluorescence.  
1167 *Remote Sensing of Environment*, 240, 111722

- 1168 Zhao, F., Dai, X., Verhoef, W., Guo, Y., van der Tol, C., Li, Y., & Huang, Y. (2016). FluorWPS:  
1169 A Monte Carlo ray-tracing model to compute sun-induced chlorophyll fluorescence of  
1170 three-dimensional canopy. *Remote Sensing of Environment*, 187, 385-399  
1171